

1 INTRODUCTION

Nova eruptions are the result of the high-speed ejection of a turbulent mass (Casanova et al. 2016; Figueira et al. 2018) due to a thermonuclear runaway (TNR) occurring within the surface layer of a mass-accreting white dwarf (WD; see Bode & Evans 2008; Woudt & Ribeiro 2014; Starrfield et al. 2016, for recent review articles). Osborne (2015) provides a recent review of X-ray observations of novae. In these close, semi-detached, binary systems the non-degenerate low-mass donor can be a main sequence star, a sub-giant, or a red giant (see Darnley et al. 2012, for a summary). Novae that have been observed in eruption just once – the majority of systems – make up the group of classical novae (CNe), of which there are around 2000 known systems across the Milky Way and nearby galaxies. All novae are predicted to repeat (Priyalnik & Kovetz 1995; Yaron et al. 2005), and a small subset, the recurrent novae (RNe) have been observed in eruption more than once. Observed recurrence periods range from $P_{\text{rec}} \approx 1$ year (Darnley et al. 2014, for M31N 2008-12a) up to 98 years (Pagnotta et al. 2009, V2487 Ophiuchi) – although the upper end must be a selection effect.

The short inter-eruption timescales of the RNe are believed to be due to a combination of a high mass WD and a high mass accretion rate (Starrfield et al. 1988b); the RNe contain many of the highest mass WDs known. Within the Milky Way there are ten confirmed RNe, including the subclass prototypes RS Ophiuchi ($P_{\text{rec}} \approx 20$ years; with a red giant donor; see Evans et al. 2008, for detailed reviews) and U Scorpii (mean $P_{\text{rec}} = 10.3$ years; sub-giant donor; see, e.g., Pagnotta et al. 2015, and references therein). Schaefer (2010) provided a detailed review of the known Galactic RNe; this and similar work indicated that the required high mass accretion rate is in most cases provided by mass loss from an evolved donor (sub- or red giant). Pagnotta & Schaefer (2014) went on to estimate that the true RN population ($10 \leq P_{\text{rec}} \leq 100$ years; A. Pagnotta, private communication) of the Milky Way may be as high as $25 \pm 10\%$ of all Galactic novae. In recent years some very rapid recurrent novae (RRNe) have been found with mean $P_{\text{rec}} < 10$ years. The best studied is M31N 2008-12a which has undergone detected eruptions in each year from 2008 (see Darnley et al. 2014, 2015, 2016a, 2019; Henze et al. 2014b, 2015, 2018; Tang et al. 2014), with a mean $P_{\text{rec}} = 0.99 \pm 0.02$ years (Darnley & Henze 2018). Theoretical studies of RRNe point to the presence very high mass WDs with high mass accretion rates and low ejected mass (e.g., Starrfield et al. 1988b; Priyalnik & Kovetz 1995; Yaron et al. 2005; Wolf et al. 2013). Therefore, in RRNe the ejecta become transparent on a much shorter time scale (than their CN counterparts), which opens the opportunity to study the evolution of the underlying system just after the eruption.

Extragalactic systems with their known distance often prove more suitable environments for the study of nova populations, and our near neighbour M31 is by far the best studied example (see Darnley & Henze 2018, for a recent review). M31 has an observed nova rate of 65^{+16}_{-15} year⁻¹ (Darnley et al. 2006) and over 1100 suspected novae have been discovered in that host alone (see Pietsch et al. 2007; Pietsch 2010, and their on-line database¹). Shafter et al. (2015) compiled a catalogue

of 16 M31 RNe and indicated that up to a third of M31 nova eruptions may be due to recurrent novae ($P_{\text{rec}} \leq 100$ years). Using an independent approach, Williams et al. (2016) indicated that $30^{+13}_{-10}\%$ of M31 novae harboured red giant donors – with an implication of a high mass accretion rate – and that these systems were strongly associated with the disk of M31. Although Nova LMC 1968 (N LMC 1968), the subject of this paper, was the first *confirmed* extragalactic nova, (see Section 2), Shafter et al. (2015) reported that the M31 nova M31N 1926-06a (Hubble 1929) was the first extragalactic nova to be observed to recur (as M31N 1962-11a; see Rosino 1964; Börngen 1968; Henze et al. 2008).

The first nova in the Large Magellanic Cloud (LMC; LMCN 1926-09a) was reported by Luyten (1927). Since then there have been 49 LMC nova candidates (see Shafter 2013, and on-line catalogue¹), around half of which have been spectroscopically confirmed. Mróz et al. (2016) recently computed the global nova rate of the LMC to be 2.4 ± 0.8 year⁻¹. Within the LMC there are four known recurrent novae, YY Doradus (LMCN 1937; Bond et al. 2004; Mason et al. 2004b), LMCN 1971-08a (Bode et al. 2016), OGLE-2018-NOVA-01 (LMCN 2018-02a; Mroz & Udalski 2018) and Nova LMC 1968 (Shore et al. 1991). Shafter (2013) concluded that $\sim 10\%$ of LMC novae are recurrent, and that $\sim 16\%$ of observed LMC eruptions occur from RN systems, though uncertainties are large since these numbers are based on four RN only. For comparison, 22 nova candidates have been discovered in the Small Magellanic Cloud¹ which with its known distance provides good multi-spectral coverage opportunities (Aydi et al. 2018). Mróz et al. (2016) compute a nova rate of 0.9 ± 0.4 year⁻¹. There are no known RNe in the SMC.

The geometry of novae ejecta is non-spherical. Axially symmetric geometries were first discussed by Gaposchkin (1957). Morpho-kinematical emission line profile modelling with SHAPE² (Ribeiro et al. 2013a,b) shows bipolar geometries. Recent Monte-Carlo based radiative transfer models of ejecta far enough after the eruption to ensure low densities and frozen-in state provide good fits to cone-shape geometries (Shore et al. 2013a,b, 2016) and can include embedded dust (Shore et al. 2018).

If a carbon-oxygen (CO) WD approaches and passes the Chandrasekhar (1931) mass a type Ia supernovae (SN Ia) thermonuclear explosion may ensue (see, e.g., Whelan & Iben 1973; Hillebrandt & Niemeyer 2000; Livio & Mazzali 2018), whereas accreting oxygen-neon WDs are predicted to collapse to neutron stars (see, e.g., Gutierrez et al. 1996). Novae have long been a proposed SN Ia progenitor pathway; the two difficulties have been the unknown composition of the massive WDs found in RNe, and the relatively low number of systems. However, recent work by Hillman et al. (2016) has indicated that an accreting CO WD can grow from its formation mass ($< 1.1 M_{\odot}$) up to the Chandrasekhar mass with little or no tuning of the system parameters (see also Hernanz & José 2008; Starrfield et al. 2012), whereas work by Pagnotta & Schaefer (2014); Shafter et al. (2015); Williams et al. (2016) has indicated that the underlying size of the RN population may be larger than first determined, as may be the global nova rates themselves (also see Chen et al. 2016; Shara et al. 2016; Soraisam et al. 2016; Shafter 2017).

¹ <http://www.mpe.mpg.de/~m31novae/opt/>

² <http://bufadora.astrosen.unam.mx/shape/index.html>

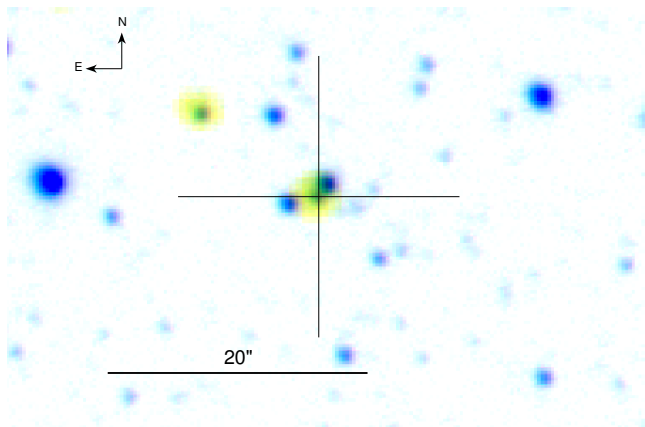


Figure 1. The finding chart of the nova. North is up and East is to the left. RGB inverted composite of UVOT *uvm2* (yellow), OGLE *I*-band (magenta), V-band (cyan). The black cross marks the nova position.

In this paper we present panchromatic observations, from the near infrared to the X-ray, of the 2016 Jan. eruption of the rapidly recurring N LMC 1968. We also revisit observations from previous eruptions. In Section 2 we provide a summary of the eruption history of the system. In Section 3 we present the observations, give the orbital ephemerides, the light curve and X-ray data analyses. In Section 4 the WD mass, reddening, secondary star, the discovery of a recombination wave in Fe^+ , and narrow line profiles are discussed. In Section 5 an estimate of the mass ejected, He mass addition from H burned during the SSS phase, orbital inclination, and accretion disk formation are discussed in the context of a comprehensive model. Section 6 provides a brief summary of some of the main points and a table summarizing the derived parameters.

2 THE RECURRENT NOVA LMC 1968

N LMC 1968 (originally referred to as Nova Mensae 1968; Sievers 1970) was first discovered in eruption at a magnitude of $m_{\text{pg}} = 10.9$ on Bamberg plates taken by I. Paterson on 1968 Dec. 16.5 UT. By virtue of its decline rate of 0.5 mag d^{-1} (see Section 3.3), the speed class (see Gaposchkin 1957) of this eruption was classified as ‘fast’. The best estimate for the onset of the 1968 eruption is $\text{MJD } 40206 \pm 1$ (Sievers 1970). Subsequently, this nova has been seen in eruption a further four times, most recently in 2016 Jan. The 1990, 2002, and 2010 eruptions are summarised below, and the 2016 eruption is introduced.

2.1 Nova LMC 1990b

On 1990 Feb. 14.1 UT (MJD 47936.1) Nova LMC 1990b was discovered in eruption at $m_{\text{pv}} = 11.2 \text{ mag}$, close to the position of N LMC 1968 (Liller 1990), see Fig. 1 for a recent finder chart. A direct comparison of the Nova LMC 1990b position to that of N LMC 1968 using the original photographic plates showed a match in R.A. within $2''.4$ and in Dec. within $6''$ (Shore et al. 1991). The peak time of eruption is more

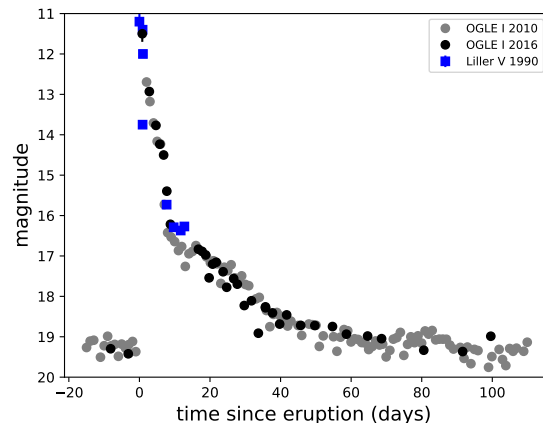


Figure 2. A comparison between the OGLE *I*-band data from the 2010 and 2016 eruptions of N LMC 1968. The V-band photometry from Liller et al. (2004) of the 1990 eruption is included as blue squares.

difficult to establish, as the last pre-eruption observation was on 1990 Feb. 3 (Liller et al. 2004), 11 days pre-discovery. However, the photometry matches that of later eruptions well (see Fig. 2) and based on that the discovery time would be within 0.2 d of the eruption.

Optical spectra of the 1990 eruption were obtained by Shara and Moffat (Williams et al. 2003) providing confirmation of the nova, thereby identifying Nova LMC 1990b as the first *spectroscopically confirmed* extragalactic RN and on day 9 by Williams et al. (2003) at the Cerro Tololo Inter-American Observatory (CTIO) in Chile. Sekiguchi et al. (1990) obtained photometry and spectra on days 8.7, 9.7, 11.7, and 15.7 at the SAAO in Sutherland, South Africa. Judging by the comparison of the 1990 magnitude at discovery to the well-observed 2010 and 2016 light curves, the (now lost) discovery spectrum was likely obtained within a day post-eruption though no time was reported in the IAU Circular 4964 of 15 Feb. 1990. The discovery spectrum showed He I and He II 4686 \AA lines with expansion velocities of 5500 km s^{-1} , and broad double-peaked Balmer lines (Williams et al. 2003), which “one tends not to see that shortly after eruption” (R. E. Williams, private communication). The 1990 eruption was deemed to be spectrally similar to the Galactic recurrent nova U Sco, with a similarly fast evolution.

Nova LMC 1990b was well observed with the International Ultraviolet Explorer (IUE) satellite which covered the eruption in the $1050\text{--}3250 \text{ \AA}$ wavelength range starting just 2 days after the discovery of the 1990 eruption, and observing on days 3, 5, 9, 14, 32, and 38 (Shore et al. 1991). The He/H ratio derived from the IUE spectra by Shore et al. (1991) was exceptionally high and seen as evidence for an evolved companion. The total UV luminosity was shown by Shore et al. (1991) to be large, possibly exceeding the Eddington luminosity for a Solar mass WD. Shore et al. (1991) used a value of $E(B - V) = 0.15 \text{ mag}$ and the Fitzpatrick extinction curve (Fitzpatrick 1986) and thus applied an extinction correction larger than we currently believe is correct (see 4.3). Since 1990, the LMC distance has also been revised

downward from 55 kpc to 49.59 ± 0.60 kpc (Pietrzyński et al. 2013; Bhardwaj et al. 2017; Pietrzyński et al. 2019), which is the distance we adopt in this paper. We revisit below the question of the luminosity in light of the reduced extinction and distance. Shore et al. (1991) derived an accretion rate $M_{acc} \geq 10^{-8.6 \pm 0.5} M_{\odot} \text{yr}^{-1}$ based on an estimated mass ejection of $M_{ej} = 10^{-7.3 \pm 0.5} M_{\odot}$ which may have been overestimated; the mean velocity width of the UV lines (FWZI) was $12,000 \text{ km s}^{-1}$ with a FWHM of 5000 km s^{-1} . The paucity of optical spectra of the 1990 eruption left open the question of whether the UV-optical derived He/H ratio was probing the same region of ejecta as the optical observations.

2.2 Missed eruptions?

The nova was almost continuously observed by the MACHO microlensing survey (Alcock et al. 1992, 2000) during the years 1993–1999 and there is no evidence for further eruptions in the available data. Eruptions of N LMC 1968 last ~ 50 days; however the initial decline essentially takes 15 days. There are a few gaps in the MACHO data as long as 40–60 days and there is thus a small probability that the nova erupted during these gaps. The limit for the MACHO observations in the LMC is $V \approx 18$ (the LMC sky background is $R \approx 19.5 \text{ mag/arcsec}^2$; Alcock et al. 1999), so an eruption would be detected significantly for up to 40 days, see Fig. 2. Based on the MACHO coverage of the LMC and assuming the nova can no longer be observed 40 days after eruption, the probability for a missed eruption is just 4%.

2.3 The 2002 eruption

In 2002 the All Sky Automated Survey (ASAS-3) observed the nova region on every other day (Pojmanski 2002). On 2002 Oct. 9, 7:18 UT (MJD 52556.304) the nova was not seen, but there were positive detections of the 2002 eruption in two subsequent observations on 2002 Oct. 11, 6:08 UT with $V = 11.15 \pm 0.02$ and with $V = 14.17 \pm 0.13$ on 2002 Oct. 15, 5:20 UT. The 2002 eruption was also observed by the Expérience pour la Recherche d’Objets Sombres (EROS) group (Tisserand et al. 2007, P. Tisserand & J.-B. Marquette, private communication). Unfortunately, a useful light curve could not be extracted from the EROS data. Based on the above we conclude that the 2002 eruption peaked between MJD 52556.3 and 52558.3 (i.e., 2002 Oct. 10).

2.4 Nova LMC 2010

The next detected eruption of N LMC 1968 occurred on 2010 Nov. 21.2 UT (MJD 55521.2 \pm 1.0) with a peak observed magnitude 11.7 ± 0.3 (Mróz et al. 2014) and was discovered by the Optical Gravitational Lensing Experiment (OGLE; see Udalski et al. 2008, 2015). The coordinates of the nova were measured to be $\alpha = 5^{\text{h}}9^{\text{m}}58^{\text{s}}.39$, $\delta = -71^{\circ}39'52''.7$ (J2000) from the OGLE data, with an astrometric accuracy of $0''.1$. A detailed analysis is provided in Section 3.3.

2.5 Nova LMC 2016

The most recent eruption of N LMC 1968 was discovered by OGLE on 2016 Jan. 21.2094 UT at a reported magnitude $I \leq$

11.5 (Mroz & Udalski 2016). The previous OGLE observation on Jan. 17.2363 indicated that the nova was still at quiescence ($I \approx 19 \text{ mag}$). This eruption was assigned the internal OGLE designation OGLE-2016-NOVA-01.

The 2016 eruption must have peaked between Jan. 19.65000 UT (which is the last non-detection from the AAVSO³ database) and Jan. 21.20942 UT (the OGLE detection). The mean time is $\text{JD } 2457407.9 = \text{Jan. } 20.4 \pm 0.8$ which we define as t_0 , the best estimate of the time of eruption, see Table 1. For the 2016 eruption on $\text{JD}=2457408.709$ we estimate the magnitude, near the peak, is $I = 11.5 \pm 0.2 \text{ mag}$, close to those of previous eruptions.

2.6 A rapidly recurring nova

Given the continuing monitoring from ASAS, and OGLE, the last three detected eruptions, 2002, 2010, and 2016 were likely to be subsequent eruptions. However, it is possible that between 1968 and 1990 several eruptions were missed. Considering that we had inter-eruption intervals (going back in time) of 1887 d, 2963 d, 4621 d, and 7731 d, from the three most recent eruptions we get an estimate of $2425 \pm 540 \text{ d}$. Using the first three intervals while accounting for a missed eruption in 1996 gives a mean period of 2356 d, which suggests either 2 or 3 missed eruptions between 1968 and 1990. If we assume there were 2 missed eruptions we get a best estimate for the interval between eruptions of $P_{\text{rec}} = 6.2 \pm 1.2 \text{ years}$, (2 standard deviations) with the possibly missed eruptions centred around February 1976 and October 1982.

With $P_{\text{rec}} < 10 \text{ years}$, we can therefore consider N LMC 1968 as one of the most rapid recurrents, and comparable to the Galactic RN U Sco. With all the other extragalactic examples being in M31, N LMC 1968 is the closest RRN with accurate distance, and therefore should be studied in much greater detail.

3 MULTISPECTRAL OBSERVATIONS

3.1 *Swift* observations (UVOT and XRT)

Upon discovery of the N LMC 2016 a Neil Gehrels *Swift* Observatory (Gehrels et al. 2004) target of opportunity observation started on 2016 Jan. 23 06:40 UT (day 2.88) with the X-ray Telescope (XRT; Burrows et al. 2005) and the Ultraviolet and Optical Telescope (UVOT; Mason et al. 2004a; Roming et al. 2005) obtaining photometric data in the UV filters and UV grism spectra. Regular *Swift* observations continued until Apr. 16 (day 85.5). The final XRT detection was on Mar. 17 (day 56.1), with the remaining 5.5 ks of exposure only providing an X-ray upper limit. Due to an observing constraint⁴, there were no *Swift* data between day 14.1 and day 24.1. *Swift* observations were not continued beyond this point since by that time the XRT count rate was too low and the contamination of the photometry by nearby sources was

³ <https://www.aavso.org>

⁴ There is an area near its orbital pole which is unobservable to *Swift*, due to the requirement that the spacecraft point more than 30° from the Earth limb, which subtends an angle of $\sim 66^{\circ}$ to the orbital altitude. This pole constraint can prevent observations of a given target for several days.

Table 1. Known eruptions of N LMC 1968.

Discovery date	Positions ¹ RA, Dec (J2000)		adopted eruption dates (MJD)	discovery magnitude ²
1968 Dec. 16.5	05:10:00[06]	-71:39:05[60]	40206.0 ± 1.5	$m_{pg} = 10.9$
1990 Feb. 14.1	05:09:58.3[.5]	-71:39:51.3[6]	47936.1 ± ?	$m_{pv} = 11.2$
2002 Oct. 10	05:09:59.4	-71:39:51.5	52557.3 ± 1.0	$V = 11.15 \pm 0.02$
2010 Nov. 21.2	05:09:58.39[.01]	-71:39:52.7[.1]	55521.2 ± 1.0	$I = 11.7 \pm 0.3$
2016 Jan 21.2	05:09:58.39[.01]	-71:39:52.7[.1]	57407.4 ± 0.8	$I \approx 11.5 \pm 0.2$

1 – Positional uncertainties are given in square brackets.

2 – The discovery magnitude is not necessarily the peak magnitude.

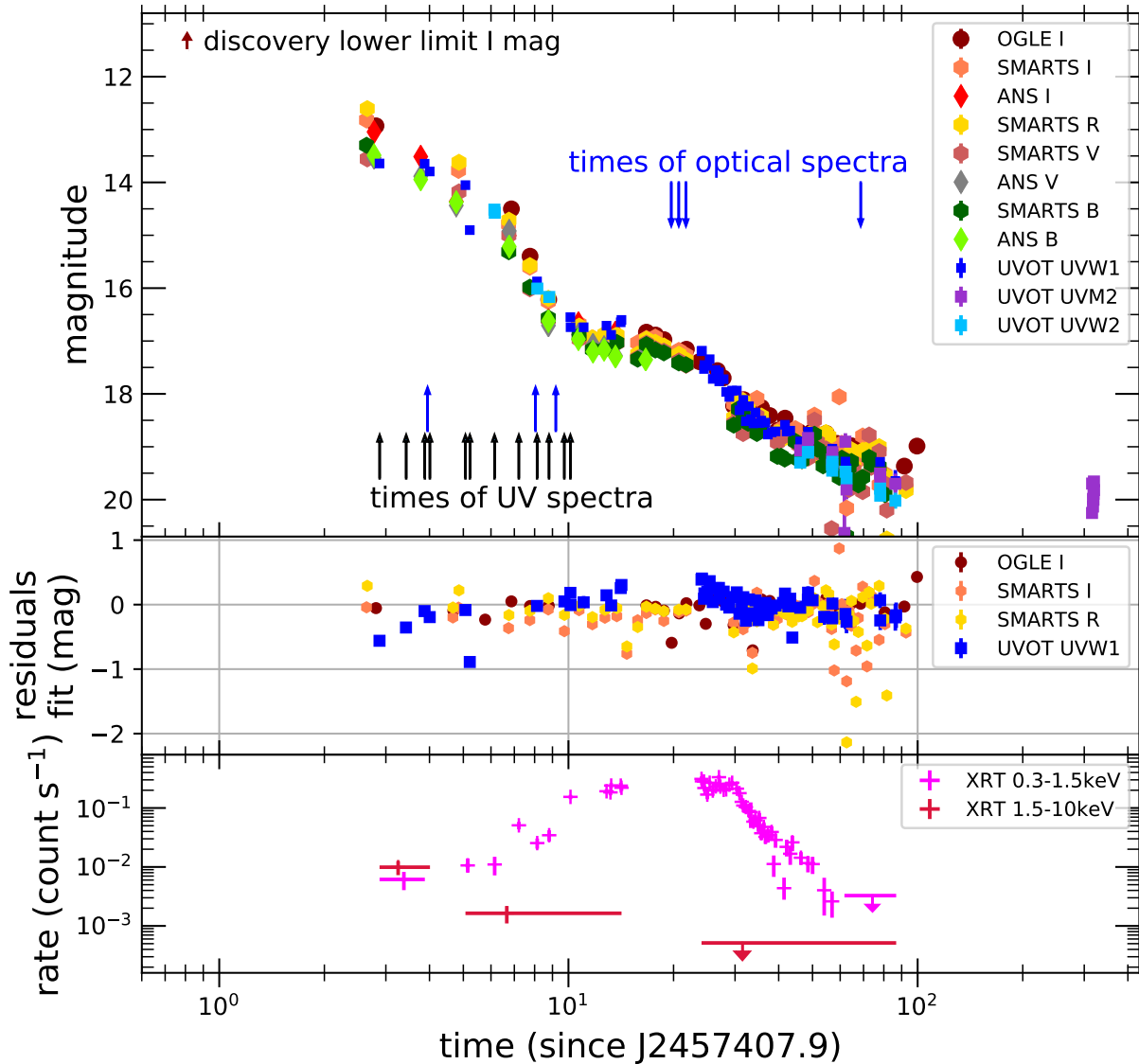


Figure 3. The optical, UV and X-ray light curves for the 2016 eruption of Nova LMC 1968. Error bars are included, but in the UV/optical are mostly smaller than the symbols. The first I-band was saturated, leading to a lower limit. In the top panel data which fell within 0.1 of orbital phase 0.0 were excluded. The middle panel shows the residuals for I , R , and $uvw1$ from the light curve fit, see Table 2; these include all observations. All panels have a common time axis where times are from the estimated eruption time. The times when spectra were obtained have been indicated. Note that the $BVRI$ magnitudes are on the Vega system but the UV magnitudes are on the AB system. The X-ray light curves for the harder and softer photons have been separated to show the initial decline in hard photons and rise in soft emission.

thought to be too large. However, additional UVOT observations were obtained on day 215–320. The processing of the *Swift* data is discussed in relation to similar multispectral data in the following sections.

3.2 XRT data reduction, the soft-X-ray light curve & variability

The *Swift* XRT observations started with a 500 s observation in Photon Counting (PC) mode. The XRT detected faint hard X-ray emission at day 4 (Darnley et al. 2016b). A significant increase in X-ray counts below 1 keV was detected on Jan. 27, only six days after discovery. This indicated the emergence of the supersoft X-ray source (SSS) emission - a phase that had never been observed before for this nova.⁵

The XRT data were processed and analysed using the standard HEASOFT tools and most up-to-date calibration files. All the X-ray data were collected in PC mode, and grades 0–12 were analysed for both the light-curves and spectra. No pile-up was evident at any time, so a circular region was used to extract the source counts, with the radius changing from 10 to 15 pixels (1 pixel $\equiv 2''.36$) depending on the brightness of the source.

Figure 3 plots the soft (0.3–1.5 keV) and hard (1.5–10 keV) band light-curves. There are very few counts above 1.5 keV, and this flux fades rapidly. The X-ray count rate was approximately constant from the day of first detection (day 2.9) until day 6.1; the soft emission then increased in brightness from day 7.2 until day 14.1, reaching ~ 0.25 count s^{-1} . At this point, the source became unobservable to *Swift*. The nova re-emerged from the observing constraint on day 24.1 at about the same count rate as ten days previously and, after a short plateau phase, started to fade from day 31. The X-ray source was no longer detected after day 57, with a final 3σ upper limit 3.3×10^{-3} count s^{-1} (0.3–1.5 keV) using 5.5 ks of data collected between 62 and 87 days.

High-amplitude X-ray variability has been observed in several novae during the early SSS phase which is yet to be fully understood (see, e.g., Ness et al. 2009; Osborne et al. 2011; Bode et al. 2016). These variations are seen to occur on time scales from hours to days. Despite daily coverage during the first 12 days of the eruption, no large amplitude X-ray variability was seen during the rise of the SSS phase in N LMC 1968.

3.3 OGLE observations

N LMC 1968 has been monitored in the *V*- and *I*-bands as part of the ongoing OGLE survey since 2010. These observations were conducted using the 1.3 m Warsaw Telescope located at the Las Campanas Observatory, Chile. All data were reduced and calibrated following the standard OGLE pipeline (Udalski et al. 2015). Both the 2010 and 2016 eruptions were discovered by OGLE; the 2010 in archival data (Mróz et al. 2014; Mroz & Udalski 2016).

The nova has a close ($\approx 1''.2$ distant) yet unrelated, bright, non-variable on-sky neighbour. Both stars are resolved in the OGLE photometry, see Figure 1 which is a colour-coded

composite image that also includes the UVOT *uvm2* band, which has a central wavelength of 2246 Å (and has a broader point spread function than the ground-based data). OGLE uses differential image techniques, so the flux is measured on the subtracted images and the effects of blending due to neighbouring stars is reduced.

Because both the 2010 and 2016 eruptions have been observed by OGLE, we can compare data taken by the same instrument for two subsequent eruptions. In Figure 2 the *I*-band light curves of the 2010 and 2016 eruptions are shown for comparison, the similarity is clearly evident. Schaefer (2010) noted that all eruptions of a given RN appear essentially identical.

Using the estimated time of eruption, we find a decrease in the *I* band of two magnitudes after $t_2 = 3.9 \pm 0.8$ d, and three magnitudes after $t_3 = 5.9 \pm 0.8$ d, see Fig. 3.

3.4 SMARTS/Andicam photometry

BVR_CIC photometry (Vega magnitudes) was obtained with the Andicam instrument on the Small and Moderate Aperture Research Telescope System (SMARTS) 1.3 m telescope at CTIO starting in Feb. 2012, monitoring N LMC 1968 twice a year (Walter et al. 2012). Daily observations of the 2016 eruption were conducted from day 2 to 81 with a break between day 22–29, further observations on day 92 and 203 and continuing. No new eruption has been seen as of $t_0 + 1174$ days.

As noted before, there are two stars in close proximity to the nova on the sky. To separate these stars, we fit three two-dimensional Gaussians to each observation using the IDL routine MPFITFUN (Markwardt 2009)⁶ constrained to have the same widths. The distribution in flux between the three stars is given by the ratios of the best fit amplitudes. Since the data are noisy, and we do not a priori know the positions of the stars, we allow the centres of the Gaussians to wander within 1 pixel ($0''.37$) of the median position.

We determined the relative positions from the fits on 14 nights, Jan. 29 through Feb. 22, excluding nights with particularly bad seeing. The contribution of the nova to the summed flux dropped from 71% to 24% during this time. Relative to the nova, the mean offset positions are: SE star: $\Delta\alpha = -2''.17 \pm 0''.06$, $\Delta\delta = -0''.34 \pm 0''.04$; NW star: $\Delta\alpha = +0''.88 \pm 0''.07$, $\Delta\delta = +1''.08 \pm 0''.08$; see Figure 1.

We calibrated the fluxes using aperture photometry in an 11 pixel ($4''.06$) aperture. We use 25 stars in the field as comparisons. They are calibrated against Landolt standard stars on photometric nights to determine their magnitudes.

3.5 ANS photometry

BVI_C optical photometry of the nova was obtained with the Asagio Novae and Symbiotic stars (ANS) collaboration (Munari et al. 2012) robotic telescope, described by Munari & Moretti (2012), located in San Pedro de Atacama (Chile). Detailed analysis of the photometric performances and multi-epoch measurements of the actual transmission profiles for the photometric filter sets in use is presented by Munari & Moretti (2012). Data reduction used the APASS sources

⁵ We checked for pre-*Swift* observations of N LMC 1968 in other X-ray and EUV mission catalogues; it was not detected.

⁶ <http://purl.com/net/mpfit>

for calibration (Henden et al. 2012; Munari & Valisa 2014) using the transformation equation calibrated in Munari et al. (2014a,b). The APASS survey is strictly linked to the Landolt (2009) and Smith et al. (2002) systems of equatorial standards.

All measurements were carried out with aperture photometry, with the aperture radius and inner/outer radii for the sky annulus χ^2 -optimized on each image to reduce dispersion of the stars in the local photometric sequences around the transformation equations from the local instantaneous to the standard system. Finally, colours and magnitudes were obtained separately during the reduction process, and were not derived one from the other. The quoted uncertainties include all error sources. Magnitudes are on the Vega system. The nearby stars contaminate the photometry due to the large ANS PSF so that the data fainter than 16th magnitude cannot be used without a correction. There are enough faint data points to be useful. To fit ANS to the OGLE and SMARTS photometry the ANS magnitude was transformed using

$$\text{mag}_{\text{corr}} = 2.5 \times \log_{10} \left[10^{-0.4(V+a)} - b \right] \quad (1)$$

with $a_I = 0.7$, $b_I = 8 \times 10^4$, $a_V = 0.3$, $b_V = 3 \times 10^{-8}$, $a_B = 0.4$, and $b_B = 3 \times 10^4$.

Munari et al. (2016) report the early *BVRI* photometry from SMARTS/Andicam and the Asagio Novae and ANS combined.

3.6 *Swift* UVOT photometry

Swift UVOT obtained UV photometry from day 2.88 until day 14, from day 24 to day 86, and from day 315 to day 320. The photometry was processed using the UVOT FT00L UVOTPRODUCT and the 20160321 version of the *Swift* CALDB. In addition a verification was made to eliminate observations that fell on areas of reduced sensitivity using the provisional small scale sensitivity map for UVOT⁷. The *Swift* UVOT filters have central wavelengths (on the AB system) of $uvw2 = 1991\text{\AA}$, $uvm2 = 2221\text{\AA}$, and $uvw1 = 2753\text{\AA}$. The filter curves and a comparison of UVOT zeropoints in AB and Vega photometric systems can be found in (Breeveld et al. 2011) and the *Swift* CALDB.

The UVOT photometric observations in the *uvw1*, *uvm2*, and *uvw2* filters are shown in Figure 3. The light curve is discussed further in Section 3.7. After day 38 there could be a possible significant contribution to the UVOT aperture from the two nearby sources. To reduce that contamination to the photometry we have used a $2''.5$ aperture, rather than the standard $5''$, with an aperture correction for count rates less than 0.5 count s^{-1} ($uvw1 < 19.72 \text{ AB mag}$). The nearby stars, which fall within the UVOT PSF, are faint in the UV and no evidence of flattening of the UV light curve is found.

3.7 The slope and breaks in the light curves

The light curves are shown on a logarithmic time scale to illustrate the temporal breaks in Fig. 3 while the rapid decline

is more apparent in the linear plot, see Fig. 2. The light curve appears to consist of a few sections each with its own power law.

For the *I*, *R*, *V*, and *uvw1* light curves we fit a function linear in magnitude, but logarithmic in time, which is equivalent to a power law fit of flux(time) since magnitude is essentially a logarithm of the flux: $m = c - s \times \log_{10}(t)$, with c a constant, m the magnitude, s the slope, and t the time. We do that initially on each section and band, find the break times from the intersections of the power laws, whereafter we repeat the fit per section. The intrinsic variability, see Fig. 3, which is also present during quiescence, makes fitting any smooth curve difficult; the measurement errors are much smaller than the variability. There appears to be a slight change in the light curves going from the red *I* band to the ultraviolet, particularly noticeable in the second slope s_2 , but generally the variabilities are so large that assuming the same evolution takes place in all bands seems acceptable. The residuals of the fit for the *I*, *R*, and *uvw1* bands in Fig. 3, middle panel, show visually the slight differences as compared to the overall evolution. The overall light curve shows several well-separated intervals, and the joint fit in Table 2 is a good representation for those. A possible explanation of the similar light curves from the UV to the IR is that the ejecta and possibly a central source are evolving as a whole because the ejecta are optically thin, while the source remains at a nearly constant temperature. This is surprisingly different from the colour evolution in CN V959 Mon (Page et al. 2013) which forms dust and in RN V745 Sco (Page et al. 2015a) which has a red giant secondary. The main difference may be the size of ejected mass.

Schaefer (2010) has pointed out that a large number of (possibly all) RNe show light curves with distinct plateau phases like we see in N LMC 1968, and suggests that as a defining characteristic of RNe. Pagnotta & Schaefer (2014) used this in a later paper in an attempt to uncover missed RNe. The plateau onset often coincides with the unveiling of the SSS.

We combined all available 2016 and 2010 *V* light curves from day 2–6 to estimate the rate of decay. When extrapolating the fit back to the estimated eruption times we obtained values of $V=12.3\pm 0.5$ at eruption, and derive $t_2 = 4.6 \pm 0.5\text{d}$ and $t_3 = 7.0 \pm 1.0\text{d}$, consistent with Munari et al. (2016) and slightly slower than in *I*.

3.8 Periodic photometric variability

The OGLE project also monitored the nova (2010–2016) whilst in quiescence. Its quiescent mean magnitudes are $\langle I \rangle = 19.29 \text{ mag}$, $\langle V \rangle = 19.70 \text{ mag}$ and colour $\langle V - I \rangle = 0.41 \pm 0.06 \text{ mag}$. Furthermore, a periodic variation (Sekiguchi et al. 1990) is seen which is interpreted as being caused by the orbital variations (see Mróz et al. 2014, for a periodogram). Henceforth we will adopt that interpretation. We obtained an optimal period of $1^{\text{d}}264329$ using the analysis of variance (AOV) statistic method (Schwarzenberg-Czerny 1996) using the 2010–2016 OGLE photometry, excluding the eruptions. The ephemeris was subsequently calculated using the O–C (observed – calculated) diagram. The cadence of the observations, at 1–2 days, is close to the orbital period, limiting the accuracy of the ephemeris.

The solution for the ephemeris for the primary minimum

⁷ http://heasarc.gsfc.nasa.gov/docs/heasarc/caldb/swift/docs/uvot/uvotcaldb_sss_01b.pdf

Table 2. Optical-UV light curve fitted parameters

band	start time (d)	t_{break} times				slope see (1)					end time (d)
		t_a (d)	t_b (d)	t_c (d)	t_d (d)	s_a	s_b	s_c	s_d	s_e	
I, I_c^3	0.81	6.2 ± 0.5	9.3 ± 0.4	21.2 ± 1.9	32.0 ± 3.4	3.6 ± 0.4	16.1 ± 0.4	0.9 ± 0.5	5.1 ± 0.3	2.1 ± 0.4	100
R	2.65	5.8 ± 0.3	9.5 ± 0.3	19.9 ± 1.9	34.7 ± 7.3	3.9 ± 0.4	13.1 ± 1.5	1.3 ± 0.6	5.8 ± 1.4	2.5 ± 0.3	93
V	2.65	6.1 ± 0.3	9.2 ± 0.3	19.6 ± 1.7	29.7 ± 9.6	2.4 ± 0.7	14.6 ± 1.4	0.6 ± 0.7	6.8 ± 3.5	2.8 ± 0.3	93
B	2.64	5.8 ± 1.2	9.5 ± 0.7	19.6 ± 2.1	34.7 ± 6.8	2.1	11.0 ± 1.1	0.9 ± 0.3	5.7 ± 0.7	1.9 ± 0.3	92.6
$uvw1$	2.88	6.1	9.8	14.5	22.5	3.9	11.4 ± 0.3	0.8	6.0	3.1 ± 0.5	86
joint ²	0.81	6.5 ± 0.2	9.2 ± 0.1	19.3 ± 0.7	38.3 ± 2.7	3.6 ± 0.3	15.4 ± 0.5	1.2 ± 0.3	5.4 ± 0.4	2.2 ± 0.2	320

- (1) We fit $\text{mag} = \text{constant} - s_i * \log_{10}(\text{time})$, beginning at the start time with slope s_a up to break time t_a , then continuing with s_b , until t_b , etc..
- (2) The joint fit of I (OGLE) I_c R_c V , B (SMARTS) $uvw1$ $uvm2$ $uvw2$ (UVOT); $uvm2$ extends to 320d normalised at $t=1.0$ d the constant for each band is $I=11.26$, $I_c=11.36$, $R_c=11.37$, $V=11.67$, $B=11.70$, $uvw1=11.43$; all with ± 0.15 mag, and $uvm2 = 10.95 \pm 0.35$, $uvw2 = 11.66 \pm 0.27$ mag.
- (3)

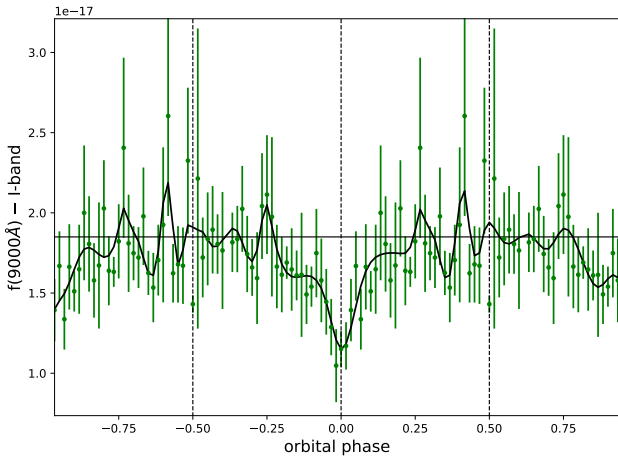


Figure 4. The I -band data folded and binned over the orbital period. The horizontal line is the mean flux for phase 0.25–0.75. The B-spline fit suggest an initial drop in brightness at phase -0.2, a further drop at phase -0.07, and a depth of the occultation of 0.40.

in the I -band is

$$\begin{aligned} \text{HJD}_{\text{ecl}} &= 2455058.323 \pm 0.090 \\ &+ (1.264329 \pm 0.000019) \times N \end{aligned} \quad (2)$$

where the errors are $1-\sigma$. The main eclipse duration is about ± 0.07 in phase and about 0.6 mag deep (a 40% decrease in flux) in the I -band, see Figs. 4 and 5. The short deep eclipse would be consistent with the WD being eclipsed.

We used the AOV method with the available data from OGLE and SMARTS starting from 23 days past the 2016 eruption (see Table 1) to determine if a period change could be detected, but we were unable to detect significant changes down at the $\pm 0^{\text{d}}.003$ error level.

Given the orbital period as derived from the I band and using the ephemeris from Eq. 2 we binned and folded our other photometry. We combined the V - and I -band photometry from OGLE and SMARTS, removing the first 50 days after the eruptions, leaving 559 data points. For V (107 data points) and B (64 data points) we also included SMARTS data from day 10 after the rapid decline stopped, while removing the trend. For the R (52 data points), the UVOT

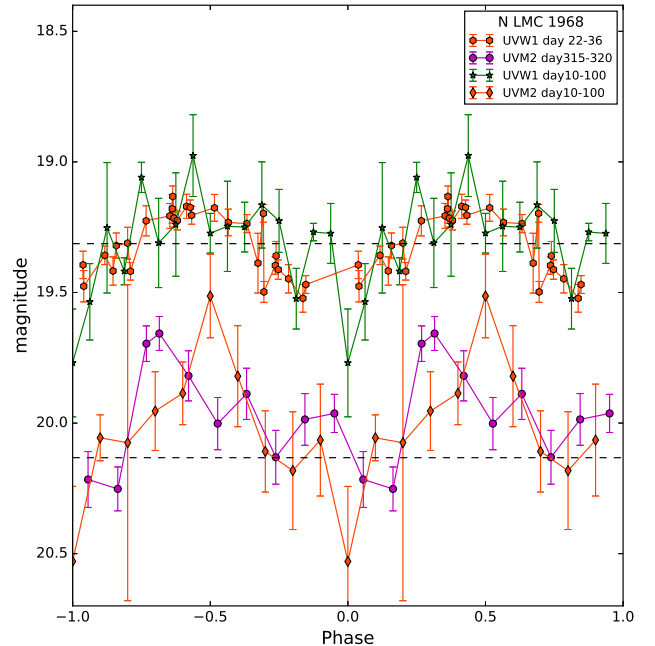


Figure 5. Light curves folded on the period of 1.264d. On the top the average $uvw1$ from days 10–100 has been compared with day 22–36 (the time the soft X-ray emission peak). The minimum is shallow and broad. The bottom two curves compare the average for the $uvm2$ (2246Å) band from days 10–100 compared with the light curve from day 315–320 after the eruption. The differences are due to variability. The dashed line is the average magnitude for each period.

$uvw1$ (58 data points), $uvm2$ (25 data points) and $uvw2$ (14 points) bands we used data from the period of 10 days until 100 days after the 2016 eruption, again removing the trend. However, the average depth and width of the minimum are only well determined in the I band, and appear of similar depth in the other bands.

In December 2016 (day 315–320) we obtained, during 4 *Swift* observations of the nova system, ten exposures in

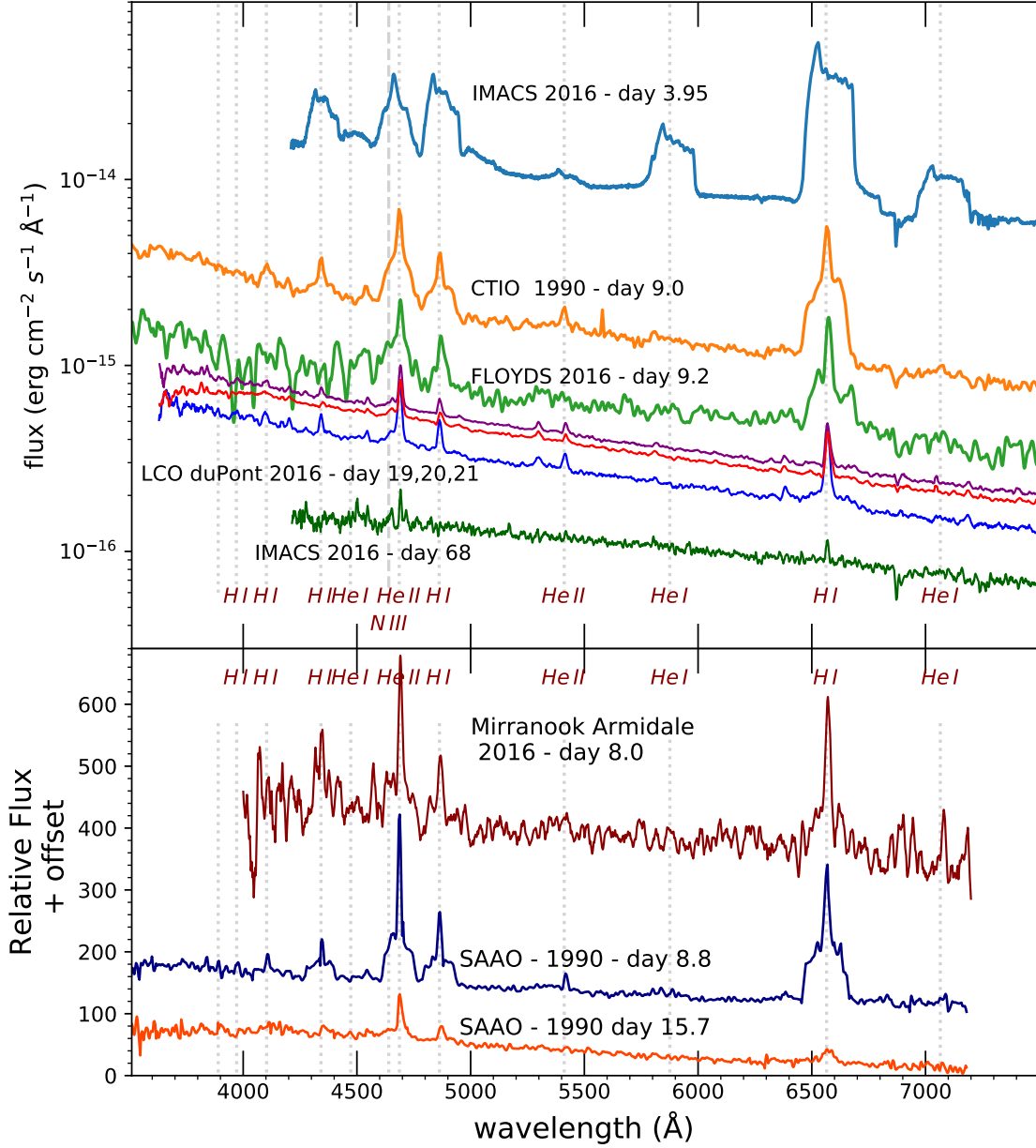


Figure 6. The optical spectral evolution of the nova in 1990 and 2016. The spectra in the top panel have a flux calibration, those in the bottom panel are not flux calibrated. We show the optical spectra from the 1990 and 2016 eruption.

the UVOT *uvm2* band only. The phased *uvm2* light curve shows an asymmetry but that is due to variability during the observation. This has been illustrated in Fig. 5 where the data is for day 46–89 (labeled day 10–100). The variability in *uvm2* appears to be mostly gradual and progressive, suggesting there slow changes in the occultation of the inner system continue long after the WD luminosity returned to the inter-eruption value.

In the *uvw1* the phased light curve for day 22–36 the occultation starts around phase -0.2, similar to the initial drop seen in the I-band B-spline fit. While the SSS phase was still on-going the *uvw1* shows nearly the same sinusoidal

profile as the long term average which suggests the presence of an accretion disk by day 28, see Section 5.3.

3.9 Optical Spectroscopy

We obtained a series of spectra at Las Campanas Observatory (LCO) of the 2016 eruption of N LMC 1968 starting with a 120s exposure on 2016 Jan 24.0345 (JD 2457411.5345, day 3.95) using the IMACS Short-Camera instrument on the 6.5m Magellan-Baade Telescope (Di Mille et al. 2016). We obtained 600s+2×1200s long exposures on 2016 Feb 8, and 3×1200s on 2016 Feb. 9 and 10 (days 19–21) on the 2.5m du Pont telescope using WFCCD/WF4K-1, and finally exposing

for 900s on Mar. 29 (day 68) with the IMACS Short-Camera, see Table A1. Spectral resolution is $\sim 5\text{\AA}$ for the IMACS data, and $\sim 8\text{\AA}$ for the WFCCD. We used standard IRAF routines to reduce the LCO spectra of the nova as well as those of spectrophotometric standard stars observed on the same nights for the flux calibration.

The first 2016 spectrum shows a moderately blue continuum dominated by broad Balmer, He I (triplet) and He II emission lines, see Figure 6. The lines have a FWZI of about $10,000\text{ km s}^{-1}$, implying velocities of 5000 km s^{-1} and present jagged profiles. A bright narrow emission peak at a velocity of $\sim 1600\text{ km s}^{-1}$ is clearly visible on the blue edge of the Balmer and He I lines, but there is no narrow centered component on the lines as seen day 8 and later. The He II 4686\AA line appears to have a more symmetric profile, which is due to a blend with the Bowen C III and/or N III lines.

A spectrum ($4000\text{--}7200\text{\AA}$) was obtained on 2016 Jan. 28 starting at 10:17 UT (day 8.0, phase 0.73) with $11\times 300\text{s}$ exposure at the Mirranook Armidale site using a LISA spectrograph on a C11 telescope with a $23\text{ }\mu\text{m}$ wide slit (about $3''$ on the sky). The spectrum shows the $H\alpha$, $H\beta$ and He II 4687\AA lines, and the lines feature narrow components.

Further spectra were obtained using the FLOYDS instrument⁸ on the 2.0 m Faulkes Telescope South at Siding Spring Observatory, NSW, Australia on 2016 Jan. 29.6 UT. (JD 2457417.1, day 9.2, orbital phase 0.63). We obtained a series of spectra 3×900 seconds long. The spectral range covers 3200\AA to $1\text{ }\mu\text{m}$ at a resolution of $R\approx 550$. The signal-to-noise of the combined spectrum is particularly low and only four emission lines are clearly visible, $H\alpha$, $H\beta$, He II (4687\AA), while the He I lines are no longer seen. The $H\alpha$ line consists of a bright narrow central peak with FWHM $= 1900\pm 100\text{ km s}^{-1}$ on top of a broader pedestal with FWZI $\approx 10,000\text{ km s}^{-1}$. We calibrated the spectrum using the mean fit to the photometry given in Table 2.

In Fig. 6 the SAAO spectra from the 1990 eruption also show a centered narrow line component on day 8.78 and 15.73 similar to that seen in 2016, but the underlying broad ‘pedestal’ of the line profiles shows a different profile in 2016 than in 1990.

Table A1 gives an overview of all the spectra, including the orbital phase.

3.10 *Swift* UV spectroscopy

Daily *Swift* UVOT UV grism spectra were obtained between 2016 Jan. 23 06:40 UT (day 2.875) and 2016 Jan. 29 (day 9).

The first grism observations consisted of two 500s segments with different roll angles in order to have a different zeroth order contamination from field stars. The details of the UVOT spectra have been given in Table A1 and A2. The spectra were processed using the calibration of Kuin et al. (2015) and code described in Kuin (2014). The calibration used includes the preliminary 2017 update to the sensitivity loss which affects the spectra below 2000\AA .

After extraction, the UVOT spectra were validated since the UVOT grism images need careful analysis (see Shore et al. 2018, for details). The grism images were compared to the star field and contaminating zeroth orders were flagged.

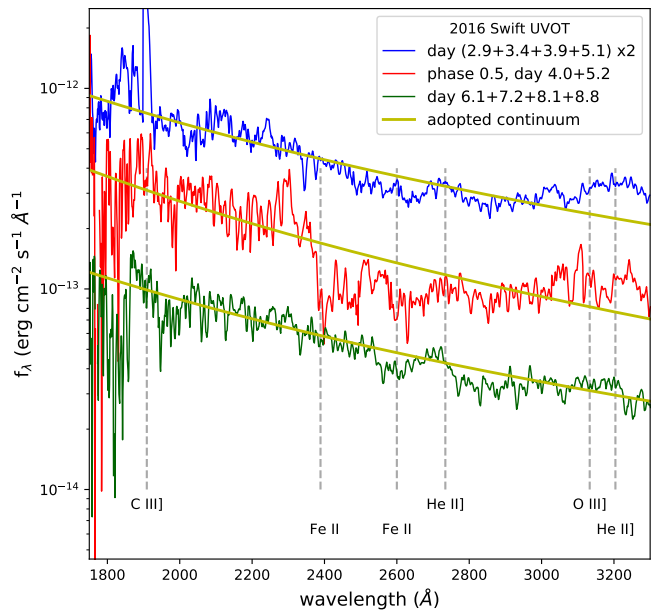


Figure 7. The observed *Swift* UVOT UV spectrum. The spectra were summed to improve S/N, weighted by the flux error. Since the early spectra are brighter, they will tend to dominate. The spectra past day 6 were taken at an offset and do not suffer from second order overlap which raises the continuum level in the earlier spectra above 2800\AA . A power law continuum has been fit to illustrate the presence of Fe II absorption features which are more prominent at phase 0.5, days 4–5.2. There are many Fe II lines in the $2380\text{--}3020\text{\AA}$ band; the UV 1 and 2 multiplet locations have only been indicated. A reddening correction for $E(B-V) = 0.07$ was applied to the spectra, see Section 4.3 and the earliest spectrum was multiplied by two for clarity. The spectra show lines of He II 2734 , 3204 , O III 3133 , and C III] 1909\AA .

This was especially important for the first six spectra because no offset on the detector was used (see Table A2).⁹ Though the UV grism spectrum from day 6.14 (phase 0.22) was unusually bright when compared with the longer term trend, it was found to be consistent with the photometry taken right before and after the spectrum showing that a brightening was taking place at that time. In order to correct for errors in the wavelength fiducial point (the anchor point, see Kuin et al. 2015) which applies equally to all spectra on a grism image, spectra of a bright nearby F5 star were extracted and used to determine a correction.

The spectra were very noisy, so we summed them to enhance the UV line emission. However, it was clear that spectra near phase 0.5 were different, while the other spectra were essentially the same, so these were summed separately. In Fig. 7 the spectra near phase 0.5 have been shown together with earlier and later summed spectra. We found weak broad lines of He II 2734 and 3204\AA , consistent with the optical spectra. A bright line appears to be present at $\sim 1909\text{\AA}$ due to C III]. We were unsure if the loss of flux below 1850\AA in all spectra is due to absorption or to the calibration of

⁸ <https://lco.global/observatory/instruments/floyds/>

⁹ The advantage of using an offset position on the detector around (1000,1600) is no second order overlap while zeroth order contamination is restricted to below 2000\AA .

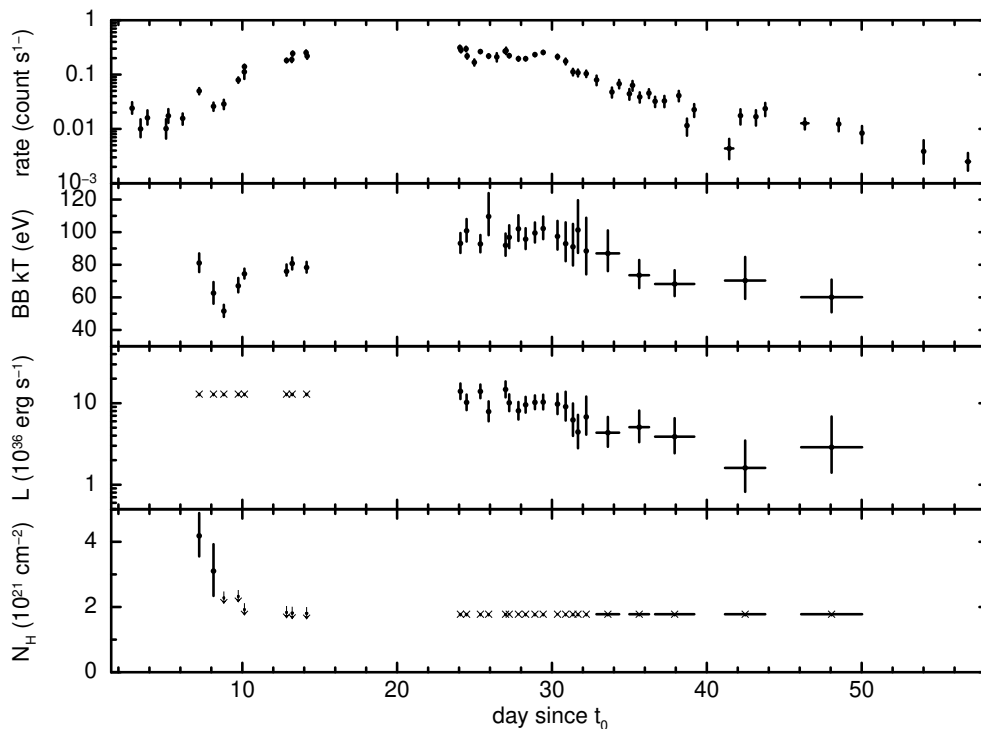


Figure 8. Top panel : The observed light curve over the full XRT band (0.3–10 keV). Second panel: The temperature of the blackbody fit to the soft spectrum. Third panel: For times > 14 d: The estimated bolometric luminosity of the BB, assuming a distance of 50 kpc; for early times L_x has been set to the mean from day 20–30. Fourth panel: Prior to day 14: the estimated N_H column. After day 14: the adopted $N_{H,ISM}$ value based on a fit to the spectra past day 20.

the sensitivity loss which is particularly difficult where the response falls to zero. We also noted a broad line which we identify as the Bowen O III 3133 Å line which is pumped by He II, consistent with the appearance of the C III/N III Bowen lines at 4630–4650 Å. Since we do not see strong UV line emission, the ejecta are not in the nebular phase before day 9.

3.11 *Swift* XRT spectra

Spectra were extracted for each individual snapshot of XRT data (where a snapshot is a continuous *Swift* pointing) after the soft emission became evident (with the first good soft X-ray spectrum for day 7.2), except for data after day 33, where several observations were combined to get spectra of sufficient signal-to-noise. A single spectrum was also extracted for the early, pre-super-soft-source (SSS) emission (days 2.9–6.1). The spectra were binned to a minimum of 1 count bin⁻¹ in order to facilitate fitting using the [Cash \(1979\)](#) statistic within XSPEC.

We can expect that prior to the rise in SSS emission on day 6 the ejecta are optically thick for X-ray emission from the WD below, and the hard X-ray spectrum is due to the optically thin emission in a shock in the ejecta. After day 6 the ejecta become transparent and the WD photospheric

emission shows through. Between day 6 and the time that the X-ray emission peaks around day 14 we expect the column density to include a decreasing contribution from the ejecta above that from the ISM. At late times, absorption from the ejecta will be negligible, and we can use that to derive the ISM column $N_{H,ISM}$ from modelling our XRT spectra.

We start with determining the ISM N_H by modelling the late time spectra, day 21 and onwards. From our late time models we derive $N_H = 1.8 \times 10^{21} \text{ cm}^{-2}$. We can compare this to the LAB ([Kalberla et al. 2005](#)) 21 cm survey, separating the LMC and Galactic components, and using the total velocity range, -150 km s^{-1} to $+300 \text{ km s}^{-1}$ the column $N_{H,ISM} = 1.8 \times 10^{21} \text{ cm}^{-2}$ within a 0.27 beam¹⁰. The model value is thus consistent with the interstellar one.

The early, day 2.9–6.1, spectrum was fitted with an optically-thin thermal component (APEC), with $kT = 5.5^{+19.1}_{-2.6}$ keV, and N_H fixed at the late-time value. The 0.3–10 keV unabsorbed luminosity of this early hard component is $1.9^{+0.7}_{-0.5} \times 10^{35} \text{ erg s}^{-1}$ which is lower than the (later) soft X-ray luminosity. The model has been chosen as appropriate for shock-heated plasma emission from internal shocks and was assumed to be unabsorbed by the ejecta.

¹⁰ <https://www.astro.uni-bonn.de/hisurvey/profile/index.php>

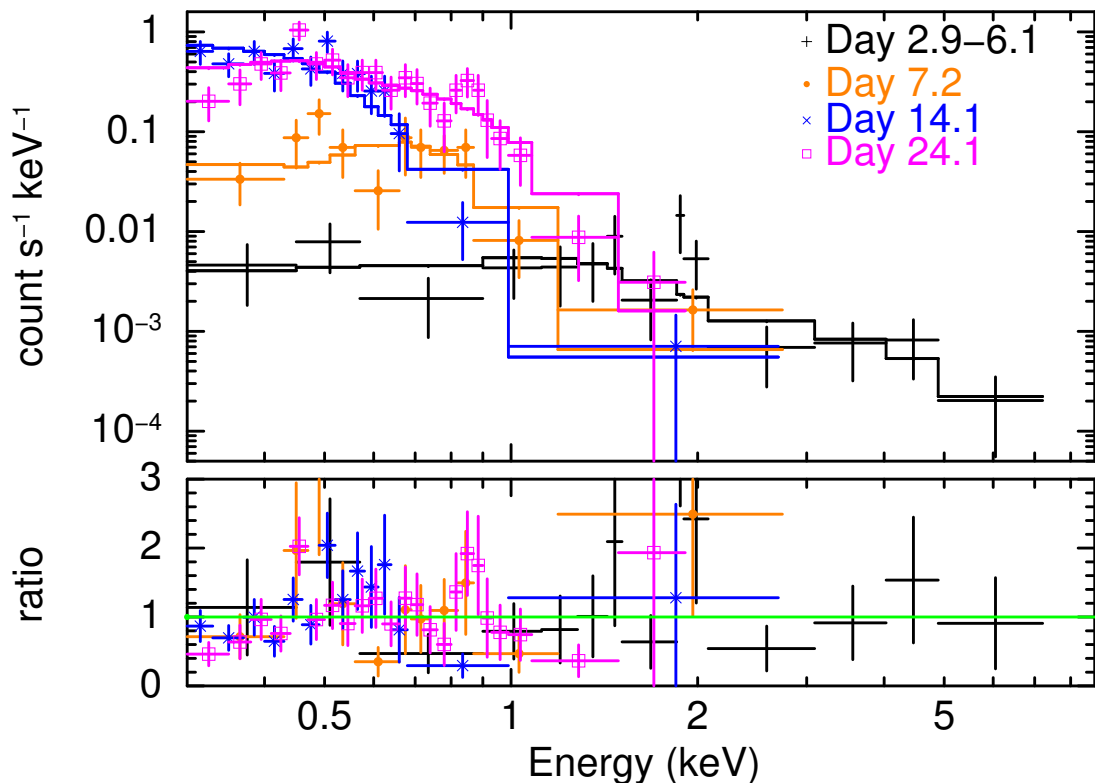


Figure 9. A sample of the Swift-XRT spectra fitted with a BB model. The lower panel shows the ratio between the data and model.

During day 6–14 we observe a rise in the XRT count rate due to the increase in the soft component. Since there are very few counts above ~ 1.5 keV after day 6, a model consisting of an absorbed blackbody (BB) component was sufficient to parametrise the SSS spectra. While a WD model atmosphere, such as the Tübingen Non-Local Thermal Equilibrium Model Atmosphere Package (TMAP¹¹) would be more physically appropriate, the temperatures required by these XRT spectra were typically too high for these model grids. We assume that the SSS emission originates from the hot WD photosphere and that the rise in SSS is due to the ejecta becoming transparent as proposed by Krautter et al. (1996) and Shore et al. (1996). We make the further assumption that the WD X-ray luminosity is constant from the eruption until the end of the SSS phase (Krautter et al. 1996). We find the bolometric luminosity of the soft X-ray source by using the mean value during the SSS plateau from a fit with N_{H} fixed to the ISM value during day 20–30, i.e., $L_{X\text{-}Bol} \approx 1.1 \times 10^{37}$ erg s⁻¹, and use that for the model prior to day 14 when N_{H} is high¹². During day 6–14 we assume N_{H} includes an additional component due to the optical thickness of the ejecta and fit a blackbody model leaving N_{H} to vary with a lower limit set by the interstellar medium value $N_{\text{H-ISM}}$. The result is shown in Fig. 8 where we see that indeed the column density shows a steep decrease from $N_{\text{H}} > 4 \times 10^{21}$ cm⁻² to the ISM value over approximately a

three day period prior to the SSS ramp up. Using the fitted blackbody temperature (~ 100 eV) and the fixed luminosity (1.1×10^{37} erg s⁻¹), we derive a BB radius of ≈ 3270 km for the hot photosphere of the WD during the peak SSS emission. There are some caveats: (1) the assumption of a BB spectrum may not be valid and the temperature may not have the usual physical meaning; (2) the system is eclipsing, so the rim of the accretion disk may hide part of the WD emission; and (3) the theoretical radius of a $1.3 M_{\odot}$ WD is smaller than 2800 km (Carvalho et al. 2018), which suggests the error in the blackbody temperature estimate is of order 8%.

Figure 9 shows a comparison of four spectra obtained throughout the rise to peak count rate. The first spectrum, up to day 6, is hard, as described above. On day 7.2 the ejecta have started to clear though the value of N_{H} still exceeds the ISM value. Despite the count rate being very similar before and after the pole constraint gap, days 14.1 and 24.1 show very different spectral shapes. The BB fit shows the later spectrum being about 20 eV hotter. That suggests that the radius of the WD photosphere decreased by about 30% between day 14 and day 24.

In Fig. 8 the fitted luminosity is found to be an order of magnitude lower than the Eddington luminosity for a $1.3 M_{\odot}$ WD, which is 1.6×10^{38} erg s⁻¹. The spectral hardening on day 24.1 takes place at the end of the plateau in the optical light curves which break around day 19.3, see Table 2. Assuming a blackbody spectrum for the SSS source the soft X-rays do not contribute significantly to the UV-optical emission. Therefore, to derive the bolometric luminosity the contemporary UV-optical/IR emission needs to be added to the L_x from the BB fit. We come back to the luminosity in Section 5.6.

¹¹ http://astro.uni-tuebingen.de/~rauch/TMAP/flux_HHeCNOFeMgSiS_gen.html

¹² The modelling choices made here are made because the fitted parameters are not completely independent, and optimising just on the goodness of fit may result in unphysical values

3.12 IUE, CTIO and SAAO data of the 1990 event

The International Ultraviolet Explorer (IUE) spectra we retrieved are from the IUE Final Archive which improved upon the earlier spectral extraction (Nichols & Linsky 1996), see Fig. 10. The long wavelength (LWP) IUE spectra cover 1900–3200Å, comparable to the UVOT UV grism, but suffer from much noise and weak emission lines. The strongest line often seen is C III]. The shorter IUE wavelength band (SWP) contains strong emission lines from C, N, and O, and H Ly α . For the IUE spectra, as well as the spectrum of N LMC 1990b taken with the 1.9 m telescope at the South African Astronomical Observatory (SAAO) in Sutherland and for the spectrum which was taken at the Cerro-Tololo Interamerican Observatory (CTIO) we can use the OGLE ephemeris from Eq. 2 for attaching an orbital phase to the 1990 outburst observations with an uncertainty of ≈ 0.15 in phase derived from the uncertainty in the ephemeris, see Table A1. With this uncertainty in the assigned phase for the 1990 observations in mind, we proceed to use them in our interpretation of the nova.

4 OBSERVATIONAL RESULTS

4.1 The companion star

Mróz et al. (2014) suggested that the period can in principle be twice that given above. However, the UV spectrum at phase 0.5, day 4 and 5.2 showed an increase in Fe II absorption. Though this is due to an ionisation effect, (see Section 4.5), it could also be associated with extra mass present outside the L2 point. The orbital period suggests that for a Roche-lobe filling secondary, the secondary must be evolved (Shore et al. 1991; Mróz et al. 2014).

We checked the pre-eruption WISE IR data for insight into the contribution from the companion. However, a comparison with the higher resolution OGLE image, see Fig. 1, shows that there are two sources within 3'' of the nova, less than the 6''1 resolution in WISE Band W1 and the 6''4 resolution of Band W2 so that no useful information can be obtained on the companion from WISE data.

The 2016 Feb. 19, 20 and 21 LCO spectra cover the 3800–9000 Å band at phase 0.98, 0.76 and 0.51, respectively. This was at the end of the plateau in the light curve. To adjust for the brightness changes we scaled the spectra using the flux of the H α line which is formed in the ejecta. We see at phase 0.51 the whole WD-facing atmosphere and at phase 0.76 only half. After scaling the spectra at phase 0.76 and 0.51 are identical within the error, so we do not observe any difference in emission due to the heated atmosphere on the side of the secondary facing the hot WD. From these observations we derive a 3- σ flux limit for the heated atmosphere in the secondary is less than $1.1 \times 10^{-13} \text{ erg cm}^{-2} \text{ s}^{-1}$ which is negligible.

The slope of a power-law fit to the LCO spectrum on day 20 is 2.27 ± 0.03 , close to what an α -disk model predicts, supporting that the accretion disk was present.

4.2 The mass of the WD

The luminosity-temperature relations in both Sala & Hernanz (2005) and Wolf et al. (2013) show that a peak temperature of >100 eV implies a high WD mass of $>1.3 M_{\odot}$. Compared to CN eruptions, RNe have much shorter intervals during which material can be accreted onto the WD, and less is needed to get ignition. Therefore, there is less material ejected during the eruption of a recurrent system. Super-soft X-rays will only be observable when the ejecta have become optically thin (e.g. Krautter et al. 1996), therefore RNe and, by extension, high mass WDs, are expected to have both short turn-on and turn-off times for their SSS phases. This is indeed found to be the case for N LMC 1968, with turn-on and -off times of about seven days and ~ 30 days respectively. These times are completely consistent with the correlations found by Henze et al. (2014a) when analysing a sample of M31 novae. The earliest detection of a SSS so far was for V745 Sco (Page et al. 2015b), with soft X-ray emission first seen about four days after eruption. V745 Sco has a recurrence time of ~ 25 yr. The rapid RN M31N 2008-12a also showed an early turn-on of the SSS phase, six days after the nova eruption (Henze et al. 2015). The small 3270 km radius of the WD photosphere as derived from the blackbody model of the peak SSS XRT spectrum in Section 3.11 is also indicative of a massive WD with $M > 1.25 M_{\odot}$ (Carvalho et al. 2018).

4.3 Reddening

We considered several lines of evidence for determining the interstellar reddening toward the nova. We made an estimate of the reddening in the direction of the nova using the Red Clump (Girardi 2016) in the Colour-Magnitude Diagram by centroiding on a $2' \times 2'$ region around the nova (30×30 pc at a distance of 50 kpc), where the measured colour $(V - I)_{\text{RC}} = 1.02 \pm 0.01$ mag (see Figure 11). Assuming an intrinsic colour for the Red Clump of $(V - I)_{\text{RC}} = 0.92$ for LMC metallicity, the reddening is $E(V - I) = 0.10$ mag. Assuming a Cardelli law (Cardelli et al. 1989) this corresponds to $A_V = 0.21$ mag, $A_I = 0.10$ mag and $E(B - V) = 0.07$ mag. This is consistent with NED¹³ Galactic extinction calculator which gives a visual extinction of $A_V = 0.206$. For an IR-independent estimate we take N_{H} discussed before in Section 3.11 from the XRT spectral fit and the LAB 21 cm survey; the column $N_{\text{H}} = 1.8 \times 10^{21} \text{ cm}^{-2}$. This value is consistent with the reddening and $N_{\text{H}}/E(B - V)$ ratio that has been reported for the LMC (Koorneef 1982). Using the Bohlin et al. (1978) calibration this is $E(B - V) = 0.09$. For the Liszt (2014) calibration for $|b| > 20^\circ$ $E(B - V) = 0.07$. We adopt $E(B - V) = 0.07 \pm 0.01$ in this paper.

We can use the UV spectra to learn more of the reddening specific to this nova. Both the 1990 IUE LWP spectra and the *Swift* UVOT spectra cover the $\lambda 2175$ Å feature from which a lower limit to $E(B - V)$ can be derived. Using the Verbunt method (Verbunt 1987) after summing all the spectra and fitting the continuum, the Cardelli et al. (1989) Galactic extinction law was applied for various values of $E(B - V)$ using $R_V = 3.1$ and visually inspected. The bump in the

¹³ NASA/IPAC Extragalactic Database, <http://ned.ipac.caltech.edu>, based on SDSS data

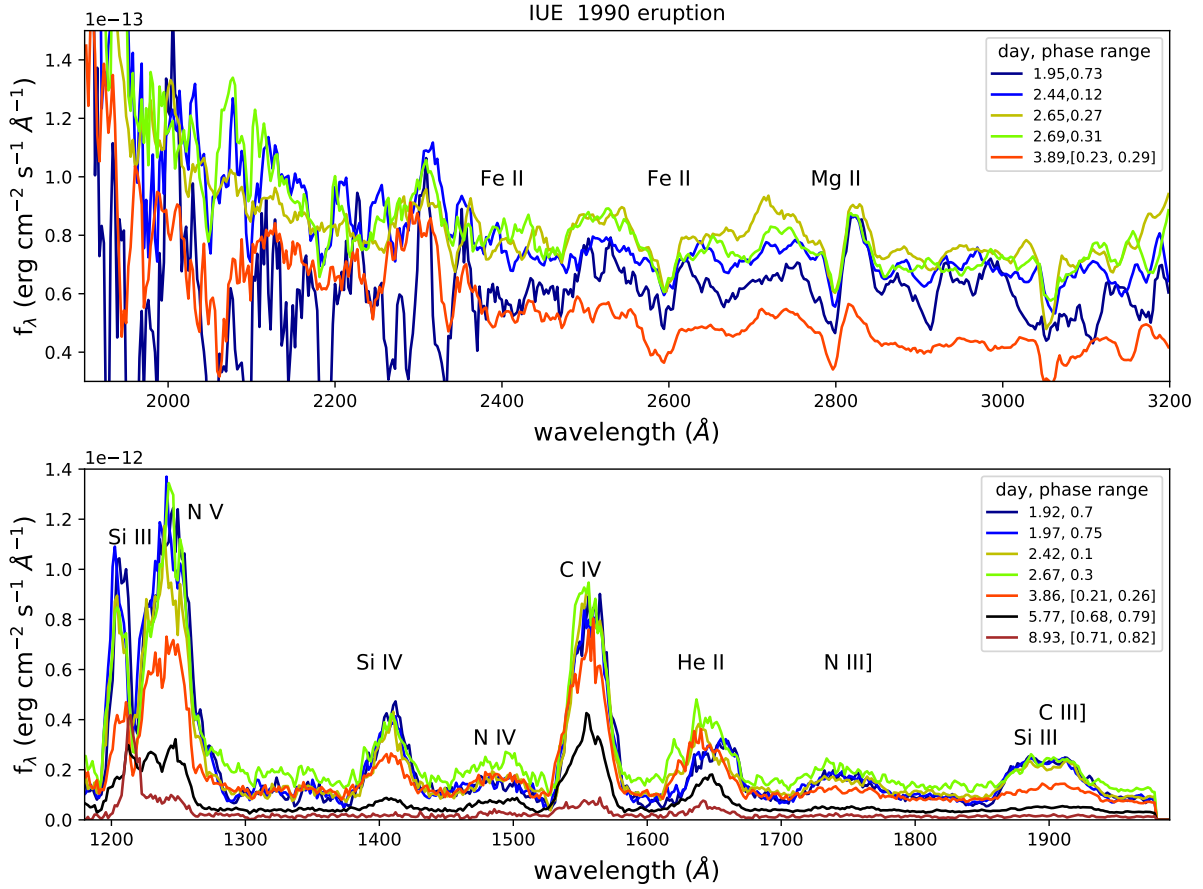


Figure 10. The IUE long (LWP) and short (SWP) wavelength spectra from the 1990 eruption. Phase is from our ephemerides. The LWP spectra show absorption of Fe II and Mg II. The LWP emission lines have been indicated. No reddening correction was applied.

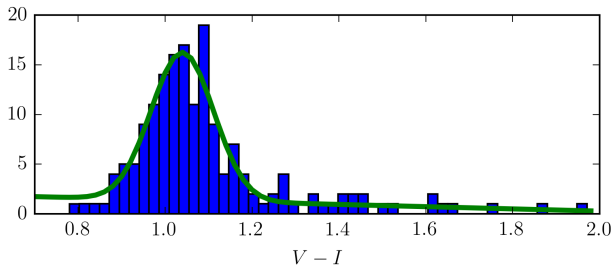


Figure 11. The histogram of the $V - I$ colour for the red clump in the Colour-Magnitude Diagram of the $2' \times 2'$ region around the nova.

spectrum (positive or negative) disappeared for a very low $E(B-V) = 0.006 \pm 0.003$, suggesting the absence of the Galactic $\lambda 2175 \text{ \AA}$ feature in that direction.

4.4 The He II line profiles variations

In the early days after the eruption opacity effects may cause shadowing of the red-shifted emission originating in the receding part of the ejecta by the approaching blue-shifted part. The suppression of the positive velocities in

the 2016 spectrum from day 3.95 shown in Fig. 12 suggest that this mechanism could be operating. However, there is another explanation: The 1990 IUE spectra, see Fig. 10, show mostly symmetric line profiles in nearly all lines except in the He II 1640 \AA line. We illustrate the evolution of the He II 1640 line profile, see Fig. 13, by normalizing to the light curve. The He II 1640 \AA profile is markedly different at orbital phase ~ 0.7 (days 1.92, 1.97) compared with phase 0.1 and 0.3 (days 2.42 and 2.67, respectively). The spectra at phase 0.7 have more emission on the red wing centred on about 1660 \AA and less on the blue wing than the spectra at phase 0.1 and 0.3. Similarly, the day 3.86 (phase 0.21–0.26) spectrum matches those of day 2.42 and 2.76 (phase 0.1, and 0.3) in peaking in the blue, but then the day 5.77 (phase 0.68–0.79) spectrum is more like the day 1.92 and 1.97 (phase ~ 0.7). The location of the peak is related to having a similar orbital phase. Such line profile changes are limited to the He II 1640 line, even though the other lines of ions with high ionisation energy (N V 1242, Si/O IV 1402/1406, C IV 1550), do not show much change to the overall profile prior to day 6, just to the flux. Hence, the asymmetric profile of He II lines in the 2016, day 3.95 (phase 0.23) spectrum may also be due to a variable component.

We conclude that in the 1990 eruption during day 2–9 the variable component of the He II 1640 emission line is tied to the orbital motion of the binary system, while the emission

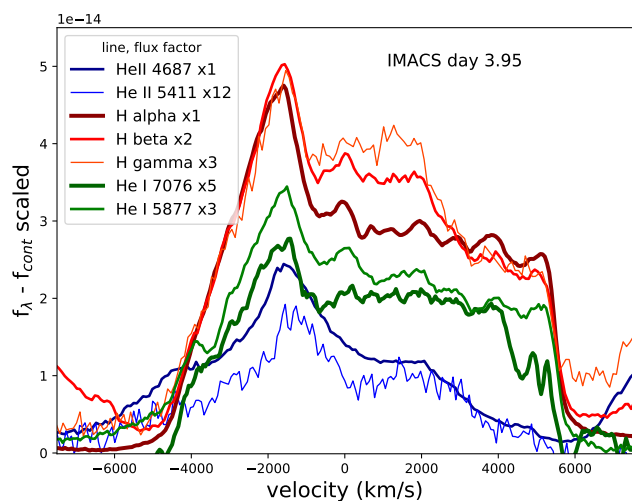


Figure 12. On day 3.95 in the 2016 outburst, the H and He line profiles in the IMACS spectrum have been displayed in velocity space. The He II lines show less emission on the red wing than the H and He I lines. Assuming symmetry, the line H and He I profile centers are at 1035 km s^{-1}

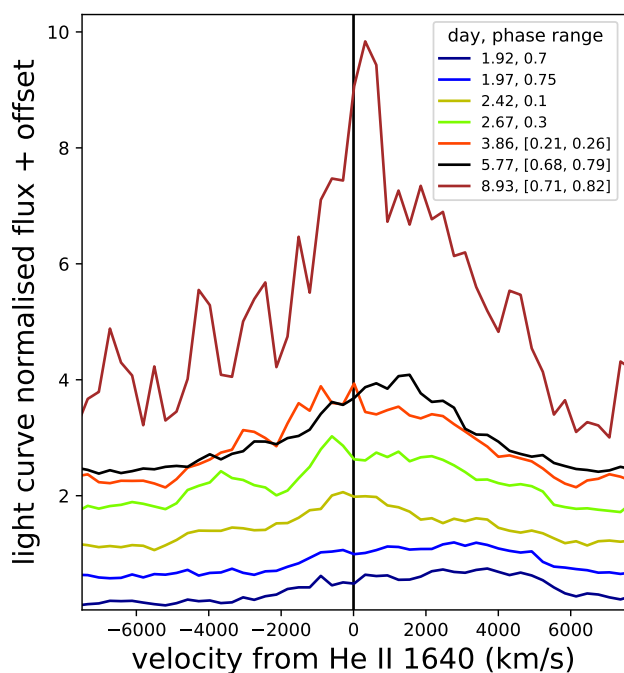


Figure 13. The changing profile of the 1990 IUE SWP He II 1640 line profile up to day 9. The flux has been normalised using the light curve fit in Table 2 and offset for clarity. The He II flux did not drop as fast as the nova brightness, and thus the earliest normalised line is the weakest, and the latest is the strongest. Note that between day 5.77 and 8.93 a central narrow line component appears. Ignoring the narrow line profile, the broader line tends to the red for orbital phase near 0.7 and slightly to the blue for orbital phase near 0.2. These line profile changes are not seen in the spectra of neutral H and He.

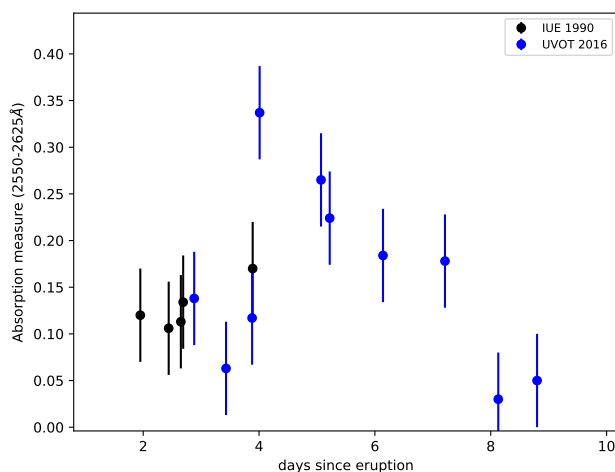


Figure 14. The relative absorption below the continuum of the region $2550\text{--}2625 \text{ \AA}$ which includes the Fe II 2600 \AA resonance line. At day 4 a recombination wave occurs.

in H, He I, and the N III, C III, C IV, and Si IV is not; those are formed in the ejecta. After day 8 a narrow component is a new addition to the He II profile; we discuss narrow profiles in Section 4.6. The variability by orbital phase in He II is possibly related to the accretion reestablishing which we discuss in Section 5.3. This might mean that the donor star is He rich (Shore et al. 1991), or that part of the WD atmosphere is ejected during the eruption but remains bound to the system.

4.5 The recombination wave in the Fe II UV 1 feature at 2600 \AA

In the UVOT spectra (Fig. 7) we see on days 4–6, evidence for Fe II absorption with features that extend over the whole range of $2300\text{--}3100 \text{ \AA}$. Inspection of the 1990 LWP IUE spectra (Fig. 10) also showed the Fe II 2600 \AA line. To better understand how this absorption is formed we determined the absorption fraction under the continuum of the reddening corrected spectra in the $2550\text{--}2625 \text{ \AA}$ band. The continuum for each spectrum was fitted with a fixed slope ensuring that the continuum was applied in a consistent way, and checking that the normalised spectra matched in the spectral regions least affected by the absorption features or emission lines. The errors were determined by varying the normalisation. The measured value is shown in Fig. 14 as a function of time after eruption.

The sudden strengthening of the Fe II absorption on day 4, and its subsequent decline to the previous level on day 9 is possibly due to a recombination wave. Recombination waves can be due to changes in opacity, temperature and ionising flux. Whilst the peak occurred around phase 0.5, earlier measurements did not match the later rise, so it is thought to be unlikely to be due to an orbital effect. After day 4 the ionising flux from the SSS phase starts to increase and cause the Fe II absorption decrease.

During day 5.2 the overall UV flux in the spectra from $1700\text{--}3000 \text{ \AA}$ is lower and the $uvw1$ photometry of day 5.22

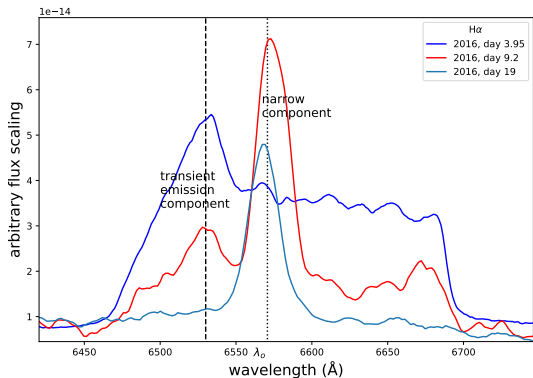


Figure 15. Sample line profile changes in $H\alpha$ during the 2016 eruption (for the full spectra see Fig. 6). Initially, the line is very asymmetric and skewed with a transient blue peak which is seen around day 4, and weakly day 8 (not shown). No narrow central peak is found until day 8; it is well-defined day 9.2 and it is still present on day 19. On day 68 it is no longer prominent. The spectra are plotted with observed wavelength, and the dotted line is the central wavelength of $H\alpha$ corrected for the systemic velocity of the LMC of 278 km/s.

is also fainter. This is probably due to the recombination wave as well.

4.6 Narrow line profile components

In our analysis we use spectra of the 1990 and 2016 outbursts. In Figures 6, and 15 a centered narrow line component can be seen in the H and He lines in 1990 and 2016 spectra after day 8 of the eruption and lasting at least till day 21.

A comparison of the 2016 FLOYDS spectrum (day 9.2, phase 0.63), of the 2016 spectrum from Mirranook Armidale (day 8.0, phase 0.73), of the first spectrum from Sekiguchi et al. (1990) of the 1990 eruption obtained on 1990 Feb. 22 (day 8.73), and the 1990 CTIO spectrum of day 9.0 (phase 0.3), Fig. 6, shows that none of them exhibits any differences in the narrow component with orbital phase.

Since the Balmer decrements show that the narrow component is due to recombination, we can expect a similar behaviour both in H and He lines and use that to determine when the narrow component appeared. Between day 4 and day 8, a 1990 IUE spectrum was taken on day 5.8, which can be compared to the IUE day 8.9 spectrum. There is a central peak present in the day 8.9 spectrum in the He II 1640 line that is not seen in the day 5.8 spectrum, suggesting that the narrow line developed between day 6 and 8 (since we see it in the day 8 optical spectrum).

Narrow components were also seen in other short period recurrent novae. A well-observed sequence can be seen in Nova LMC 2009a where the narrow component is seen to appear around day 10 and disappear when the SSS phase ends and thus the X-ray luminosity drops (Bode et al. 2016).

Williams et al. (1981) describe IUE observations of the 1979 outburst of nova U Sco where He II 1640 developed a narrow component between day 6 and 8 after discovery. Sekiguchi et al. (1988) display a sequence of spectra for the 1987 outburst which shows no narrow peak on day 4,

but it is present on day 9 and 19 after eruption. The well-observed 2010 eruption shows that on day 5 there was no central narrow component (Kafka & Williams 2011; Mason et al. 2012), while it is present on the day 5.8 spectrum and disappeared between days 33 and 41 (Anupama et al. 2013), comparable to the end of the SSS phase around day 40 (Orio et al. 2013).

RN V394 CrA, a fast nova showing similarities to U Sco, had two outbursts, one in 1947 (Duerbeck 1988), and one in 1987 (Liller et al. 1987). Spectra taken 1987 Aug. 3 and 4, 5 and 6 days after the eruption, show only a broad flat line profile in the H I and He II lines, while by 1987 Aug. 13, day 11 and later, they show a narrow line profile component in these lines which appears diminished by Sep. 15. A spectrum taken 1987 Oct. 4 shows that the narrow component has all but disappeared (Sekiguchi et al. 1989; Starrfield et al. 1988a).

The narrow lines are thus found in similar RNe systems, and are characterised by the initial absence until several days after the eruption, and disappearance at the time the SSS emission also drops off. This suggests that the narrow emission is powered by the high-energy emission from the WD, just like the soft X-rays are.

Several mechanisms have been proposed to explain these narrow lines centered on the line wavelength and on top of a broad pedestal. Almost certainly the narrow component of the line is formed in a different region from the broad pedestal which is due to the ejecta. We explore the possibility here, that the narrow component is due to reionisation of trailing clumps of cool matter from the previous eruption at distances of several 10^{16} cm. The time delay between the eruption and the appearance of the narrow lines is due to the light travel time to reionise the distant shell, assuming the UV/EUV radiation from the photosphere is sufficient even before the start of the SSS phase. The observed line width (FWHM) of $\approx 1100 \text{ km s}^{-1}$ will be due to a low gas temperature and velocity of the clumps, and is consistent with the distance reached in about seven years by the slower ejecta. The recombination time needs to be less than about a day which requires densities of $> 10^7 \text{ cm}^{-3}$ and implies a filling factor of $< 10^{-6}$. Estimated filling factors in the days after the eruption of 0.01–0.001 scale after 7 years of expansion to $< 10^{-6}$ provided the clumps do not grow faster than by thermal expansion.

We cannot reliably detect variations in the narrow component with orbital phase in N LMC 1968. Reionisation of clumpy ejecta from a previous eruption provides a possible explanation for the narrow line profiles.

5 OBSERVATIONS IN A MODEL CONTEXT

5.1 A comprehensive model

Late time spectral observations show that nova ejecta have a bipolar shape (Hutchings 1972; Mustel & Boyarchuk 1970; Solf 1983; Gill & O’Brien 1999, 2000; Harman & O’Brien 2003; Ribeiro et al. 2009; Shore 2012; Shore et al. 2013a,b, 2016), and we will assume this to be so for this nova. The visible brightness decay time scale t_3 , is shorter for smaller mass ejected and higher velocity since the ejecta become transparent faster. In the RN with a late-type secondary the

SSS X-ray emission onset is delayed from the eruption itself by a period of at least a few days (Schwarz et al. 2011). The SSS emission is likely the surface emission of the WD with nuclear burning continuing after the initial eruption for a period of weeks to months until the all the hydrogen has been burned. The upper atmospheric temperature of the WD is typically $<1\text{MK}$.

The accretion disk may have been disrupted in the initial eruption (for U Sco see Drake & Orlando 2010), though the ejected mass is low, reducing the potential for disruption. For example, in M31 N 2008-12a the accretion disk is thought to survive (Henze et al. 2018). In addition to the eruption, the high luminosity of the WD will heat the atmosphere of the secondary. For a secondary that fills its Roche lobe this leads to matter filling the inner WD Roche lobe from both the accretion disk and by overflow from the heated atmosphere. Eventually that matter will undergo a pancake-like instability and reform the accretion disk. At the same time, over possibly a large period, hydrogen is converted to helium in the layers still bound to the WD, and not lost.

Thus, in the higher mass WDs ejecta become transparent faster, reducing the time for the density of the ejecta to become low enough to observe the WD and inner system. N LMC 1968 has a very small t_3 , smaller than the Galactic nova U Sco which also has an evolved companion, similar spectra, and SSS phase, and a comparable orbital period of 1.23d (Schaefer & Ringwald 1995). In N LMC 1968 the suggestion of the changing eclipse profile, the early occurrence of eclipses, and the behaviour of He II (see Section 4.4) are all consistent with a model where debris filling up the inner WD Roche lobe initially block the WD photosphere from view, though that does not rule out that the bipolar ejecta also cross the line of sight. We'll consider the consequences of that in the following subsections.

5.2 Inclination of the orbit

It is likely that we are seeing the system at an inclination angle close to the orbital plane because we have seen eclipses. Ness et al. (2013) estimate an inclination angle of $> 76^\circ$ is to be expected for an SSe type system (which shows emission lines). Our interpretation of the UV flux variations suggests that we view close across the rim of the accretion disk, which would imply a system inclination in the $68\text{--}76^\circ$ range: Fragner & Nelson (2010) show that for a low α , thicker disk, the disk can warp and rotate rigidly, which could fit with the observed changes to the UV emission.

The SSS onset could be expected to happen sooner if the line of sight were not intersecting the bipolar ejecta, i.e., at high inclination. The presence of an accretion disk does not preclude scattering of soft X-rays in a halo above the disk. However, in such a situation the debris left in the inner Roche lobe in the days after the eruption could effectively block the X-rays and delay the SSS onset.

5.3 The accretion disk and precursor

It is unknown what happens to the accretion disk during and after the nova explosion, but N LMC 1968 may provide some insight. The main questions relating to the accretion disk are: (1) was the accretion disk destroyed in the explosion, (2) does

the Roche lobe overflow (RLOF) from the secondary change, and (3) how long until the accretion disk is restored as a steady element in the system? The hydrodynamic models from Drake & Orlando (2010) show that in the eruption of U Sco, a very similar system, the accretion disk would not survive the initial blast which seems to answer point (1). However, we do not have the data to support that. The accretion disk may very well have survived the blast; perhaps in a state where the vertical structure was no longer in hydrostatic equilibrium. As to point (2), our observations show evidence of matter bound to the system in the UV variability, in the changes to the He II profiles as early as day 2, and RLOF is possibly a factor in the delay of the onset of the SSS. As to point (3): if indeed the 'debris' is sufficiently spread out throughout the inner Roche Lobe and neighboring regions, that matter, whilst blocking the X-rays from the WD atmosphere, would need to collapse to the orbital plane to reform the initial accretion disk. Taking a look at the observations they seem to indicate the process to take 6 days, at which time the SSS starts and the gradient of the light curve steepens, in accordance to a change in the optical and UV source.

The physical process can be modeled simply by assuming that after the eruption we start reformation of the accretion disk with a messy atmosphere filling the Roche lobe around the WD. Whether this atmosphere consists of large blobs moving under gravity nearly like solid bodies or is fully turbulent, the momentum in vertical motions will dissipate with each crossing of the orbital plane, since atmospheric elements with opposite momentum will interact. We can identify the spectral signature of this turbulent material with the UV-optical spectral energy distribution (SED). The variable line components seen in He II are taken as an indication of the blob velocities of order 3000 km s^{-1} (the He II FWZI is $10,000\text{ km s}^{-1}$). With the disk formation and clearing out of the WD Roche lobe within 6 days the disk is not necessarily stationary, since the mass inflow may still evolve either from the secondary or from enhanced inflow from the heated atmosphere of the secondary. Since orbits closer to the WD mean higher velocities, dissipation of energy and relaxation times will, similarly to an accretion disk, be larger near the WD. This scenario provides an update to the simple picture of the formation of an accretion disk by Verbunt (1982) for novae.

5.4 H burned to He during the SSS-phase

During the SSS phase steady nuclear burning takes place on the surface of the WD. The burning is eventually quenched due to a drop in the temperature and pressure, which in turn happens when the hydrogen that fuels the luminosity runs low. We can assume that the steady burning occurred from the time of the explosive ejection of material until the time of turnoff. The SSS luminosity is thus a way to measure how much He is added to the WD during that period, regardless of the source of the H being pre- or post-eruption. The difference between He ejected and added due to burning during the SSS phase gives an indication of the rate of growth of the WD mass.

A blackbody fit to the X-ray spectrum shows that during the SSS phase the luminosity of the surface is $1.1 \times 10^{37}\text{ erg s}^{-1}$ (Section 5.6, Fig. 9). The downturn in the light curve starts

Table 3. Summary of the parameters for N LMC 1968

property	value	unit	Section
2016 eruption JD	2457408.709 ± 0.8		2.5
adopted distance LMC	50	kpc	2.1
minimum mag < V_{min} >	19.70	mag	
maximum mag V_{max}	12.3 ± 0.5	mag	
decay time 2 mag t_2	4.6 ± 0.5	d	3.7
decay time 3 mag t_3	7 ± 1	d	3.7
epoch binary	2455058.323 ± 0.090	HJD	3.8
period	1.26433 ± 0.000019	d	3.8
period change $\Delta P/P$	< 0.003		3.8
reddening E(B-V)	0.07	mag	4.3
interstellar N_H	1.8×10^{21}	cm^{-2}	3.11
SSS emission phase	6-57	d	3.2
SSS typical luminosity	1.1×10^{37}	erg/s	3.11
Kinetic energy	$\approx 10^{38}$	erg/s	5.6
SSS typical BB temp.(kT)	100	eV	3.11
narrow component FWZI	1.6×10^3	km s ⁻¹	3.9
FWZI broad component	10^4	km s ⁻¹	3.9
Sp. type secondary	unknown		4.1
Ejecta Velocity	5000	km s ⁻¹	3.9
WD mass	> 1.3	M_\odot	4.2
depth eclipse	0.6	mag	3.8
duration eclipse	0.05	phase	3.8
ejected mass	$\approx 10^{-7}$	M_\odot	5.5
H converted to ^4He	2.2×10^{-9}	M_\odot	5.4
system inclination	68 – 76	degrees	5.2
recurrence time	6.2 ± 1.2	years	2.6
UV-optical L(1d)	4×10^{37}	erg s ⁻¹	5.6
peak L_X (14-30d)	1.1×10^{37}	erg s ⁻¹	5.6

at day 30, so in 30 days the energy produced was 2.8×10^{43} erg. Assuming one gram of H converted to ^4He produces 6.40×10^{18} erg, the total He mass created is $M(\text{He}) = 4.4 \times 10^{24} g = 2.2 \times 10^{-9} M_\odot$. If the accreting matter were high in He, the estimated growth in WD mass is a lower limit.

In N LMC 1968 the He abundance is very high (Shore et al. 1991). This may be due to He rich ejecta or because the secondary has lost most of its hydrogen. In our proposed messy atmosphere the variable He II line component would be in the inner Roche lobe in the early days after the eruption but it is unclear how it got there.

5.5 Estimate of the ejected mass

The quiescent luminosity is thought to be dominated by the accretion disk luminosity L_{acc} . Taking the photometry from around day 70 we can construct an SED (1900–9000Å). We estimate $L_{acc} \geq 4 \times 10^{34} \text{ergs}^{-1}$ where the lower limit is because the dereddened spectrum has an unaccounted component which is still rising in the UV. This translates to an accreted mass of at least $M_{acc} \geq 3.5 \times 10^{-8} M_\odot$ using Osborne et al. (2011).

Under an assumption that the bipolar ejecta cross our line of sight, and there is no debris left in the inner Roche lobes, we can use the start time of the SSS phase to derive an estimate of the ejected mass along the line of sight, since that happens when the N_H column reaches a value where the soft X-rays become transparent while we also know at what time the SSS rise occurs. Multiplying that time with the measured ejecta velocity then gives the distance to use with

N_H . On day 7.2, $N_H = 4 \times 10^{21} \text{cm}^{-2}$, while $V_{ej} = 5000 \text{km s}^{-1}$. Of course, for extrapolating that to the total ejected mass we will have to make some estimate of the geometry of the ejecta. Since the ejecta are bipolar, the ejecta covers a solid angle Ω , and we derive an ejecta mass of $\approx 3 \times 10^{-7} (\Omega/(4\pi)) M_\odot$. Assuming the accreted mass is 2-3 times the lower limit above and a solid angle of $\approx \pi$, the numbers for accreted and ejected mass are compatible with $M_{ej} \approx 10^{-7} M_\odot$, but do not allow a determination of net mass loss or growth for the WD.

5.6 The UV and X-ray luminosities

The peak UV luminosity (1200–3300Å) of N LMC 1968 in the 1990 outburst was computed by Shore et al. (1991) to exceed the Eddington luminosity ($1.6 \times 10^{38} \text{erg s}^{-1}$ for a $1.3 M_\odot$ WD), but with our adopted smaller distance, reddening and N_H , the luminosity is nearly a factor 4 smaller: Using the SED derived from the normalisation of the light curve fit at day 1.0 (see Section 3) and fitting that with a blackbody, the peak luminosity of the UV-optical component is $L_{UV} \approx 4 \times 10^{37} \text{erg s}^{-1}$. We also tried to fit the dereddened continuum of the combined day 2 to 4 spectra using the 1990 IUE as well as the 2016 day 2.9 UVOT and day 3.95 IMACS spectra, covering 1150–9000Å, but a single blackbody fit is not possible. The UV rise suggests a temperature in excess of $\sim 25,000 \text{K}$ plus a cool component to deal with excess IR flux.

After the initial ejection, the WD luminosity becomes thermalised by the optically thick ejecta, but once the ejecta has become optically thin, the luminosity comes out in the X-ray and EUV. We found in Section 3.11 that $L_{X-Bol} \approx 1.1 \times 10^{37} \text{erg s}^{-1}$. The UV-optical light during the SSS is by then much less than near the peak: A black body fit for the UV-optical component at that time gives $L_{UV} = 2.4 \times 10^{35} \text{erg s}^{-1}$.

A review of the past eruptions suggest the rise time to peak is about a day. Using the estimate for the ejected mass and the expansion velocity, the kinetic energy rate imparted in the first day is around $3 \times (\Omega/4\pi) \times 10^{38} \text{erg s}^{-1}$, with Ω the solid angle of the ejecta. This suggests that the kinetic energy imparted the first day of the eruption is close to the Eddington luminosity, and dominates over the energy lost in radiation.

6 CONCLUSIONS

In Table 3 the main parameters which have been derived are collected.

The recurrence time of N LMC 1968 is short and we expect another explosion to happen around April 2022 ± 1.2 years. In this study we collected and interpreted the known data from which we derived the ephemeris for the WD eclipse. Though the system shows eclipses, we do not have radial velocity measurements which would help determine the orbit and mass ratio of the binary.

The radiant luminosity is found to be lower than Eddington for a He-atmosphere by an order of magnitude, unlike in many other novae. If the intrinsic luminosity of the nova is near Eddington, the lower observed value could be due to shadowing by the accretion disk, where only Thompson scattering of the X-rays in a halo above the orbital plane of the system is observed. However, the kinetic energy in the

ejecta required an Eddington luminosity during the initial TNR. This could mean that for the rapid recurrent systems the kinetic energy dominates over the observed radiative component.

We also observe evidence that suggest that prior to day 7 (after the eruption) there is a source of gravitationally bound material in the system, possibly due to increased mass flow from the secondary, disruption of the accretion disk, or part of the WD atmosphere that did not reach escape speed. This is seen as a variable He⁺-rich matter component which shows orbital periodicity day 2–7 after the 1990 eruption and could be located in the inner Roche lobe or just outside it. The eventual collapse of this matter into the orbital plane could bring about the emergence of the WD soft X-ray emission. The rise of the SSS emission could alternatively be due to the decreasing column density in the expanding bipolar ejecta.

A sudden increase in the Fe II UV absorption on day 4 is seen as evidence for a reionisation wave happening in the ejecta.

Linking the SSS luminosity to steady burning on the WD surface we arrive at an estimate of the mass of H converted to He after the eruption. This matter is adding to the WD mass, providing a link between SSS duration and growth of the WD. We also estimate the ejected mass and find that to be compatible with the accretion rate. The high SSS temperature suggests the WD mass is larger than 1.3 M_⊙.

In the UV we observe eclipses out to 320 days after the 2016 eruption which are shallow and broad while the emission is variable, suggesting that the accretion disk is not stable or is perhaps warped.

The current study has left many questions. Some of those could be answered by future high resolution multispectral observations of the different phases of the eruption, and better characterisation of the orbital parameters.

ACKNOWLEDGEMENTS

The OGLE project received funding by the National Science Center, Poland, under grant MAESTRO 2014/14/A/ST9/00121 to A.U. P.M. acknowledges support from the Foundation for Polish Science (Program START). N.P.M.K., K.L.P., A.A.B., A.P.B. and J.P.O. acknowledge support from the U.K. Space Agency. M.H. acknowledges the support of the Spanish Ministry of Economy and Competitiveness (MINECO) under the grant FDPI-2013-16933. S.S. acknowledges partial support from NASA, HST, & NSF grants to ASU. Research in Novae at Stony Brook University is supported in part by NSF grant AST 1614113, with additional research support provided by the Stony Brook University. RDG was supported by NASA and the United States Air Force. V.A.R.M.R. acknowledges financial support from the Fundação para a Ciência e a Tecnologia (FCT) in the form of an exploratory project of reference IF/00498/2015, from the Center for Research & Development in Mathematics and Applications (CIDMA) strategic project UID/MAT/04106/2019, and supported by Enabling Green E-science for the Square Kilometre Array Research Infrastructure (ENGAGE-SKA), POCI-01-0145-FEDER-022217, and PHOBOS, POCI-01-0145-FEDER-029932, funded by Programa Operacional Competitividade e Internacionalização (COMPETE 2020) and FCT, Portugal. RA acknowledges financial support from DIDULS Regular PR#17142 by Universidad de La Serena. The Swift data were retrieved from the UK Swift Data centre. IUE spectra were

retrieved from the MAST archive. This work makes use of observations from the Las Cumbres Observatory network. We acknowledge with thanks the variable star observations from the AAVSO International Database contributed by observers worldwide and used in this research. We would like to acknowledge Elena Mason, and Bob Williams for discussions, Mike Shara, Kaz Sekiguchi, and David Buckley who tried to chase down old observations of this nova, and Patrick Godon for discussions on the accretion disk. We used HEASARC Ftools, IDL, scipy, matplotlib, and astropy.

REFERENCES

- Alcock C., et al., 1992, in Filippenko A. V., ed., *Astronomical Society of the Pacific Conference Series Vol. 103, Robotic Telescopes in the 1990s*. pp 193–202
- Alcock C., et al., 1999, *PASP*, **111**, 1539
- Alcock C., et al., 2000, *ApJ*, **542**, 281
- Anupama G. C., et al., 2013, *A&A*, **559**, A121
- Aydi E., et al., 2018, *MNRAS*, **474**, 2679
- Bhardwaj A., Macri L. M., Rejkuba M., Kanbur S. M., Ngeow C.-C., Singh H. P., 2017, *AJ*, **153**, 154
- Bode M. F., Evans A., 2008, *Classical Novae*. Vol. 43
- Bode M. F., et al., 2016, *ApJ*, **818**, 145
- Bohlin R. C., Savage B. D., Drake J. F., 1978, *ApJ*, **224**, 132
- Bond H. E., Walter F., Espinoza J., Gonzalez D., Pasten A., Green D. W. E., 2004, *IAU Circ.*, **8424**, 1
- Börngen F., 1968, *Astronomische Nachrichten*, **291**, 19
- Breeveld A. A., Landsman W., Holland S. T., Roming P., Kuin N. P. M., Page M. J., 2011, in McEnery J. E., Racusin J. L., Gehrels N., eds, *American Institute of Physics Conference Series Vol. 1358, American Institute of Physics Conference Series*. pp 373–376 ([arXiv:1102.4717](https://arxiv.org/abs/1102.4717)), [doi:10.1063/1.3621807](https://doi.org/10.1063/1.3621807)
- Burrows D. N., et al., 2005, *Space Sci. Rev.*, **120**, 165
- Cardelli J. A., Clayton G. C., Mathis J. S., 1989, *ApJ*, **345**, 245
- Carvalho G. A., Marinho R. M., Malheiro M., 2018, *General Relativity and Gravitation*, **50**, 38
- Casanova J., José J., García-Berro E., Shore S. N., 2016, *A&A*, **595**, A28
- Cash W., 1979, *ApJ*, **228**, 939
- Chandrasekhar S., 1931, *ApJ*, **74**, 81
- Chen H.-L., Woods T. E., Yungelson L. R., Gilfanov M., Han Z., 2016, *MNRAS*, **458**, 2916
- Darnley M., Henze M., 2018, in 42nd COSPAR Scientific Assembly. pp E1.7–36–18
- Darnley M. J., et al., 2006, *MNRAS*, **369**, 257
- Darnley M. J., Ribeiro V. A. R. M., Bode M. F., Hounsell R. A., Williams R. P., 2012, *ApJ*, **746**, 61
- Darnley M. J., Williams S. C., Bode M. F., Henze M., Ness J. U., Shafter A. W., Hornoch K., Votruba V., 2014, *A&A*, **563**, L9
- Darnley M. J., et al., 2015, *A&A*, **580**, A45
- Darnley M. J., et al., 2016a, *ApJ*, **833**, 149
- Darnley M. J., Kuin N. P. M., Page K. L., Osborne J. P., Schwarz G. J., Shore S. N., Starrfield S., Williams S. C., 2016b, *The Astronomer’s Telegram*, **8587**, 1
- Darnley M. J., et al., 2019, *Nature*, **565**, 460
- Di Mille F., Angeloni R., Morrell N., 2016, *The Astronomer’s Telegram*, **8586**, 1
- Drake J. J., Orlando S., 2010, *ApJ*, **720**, L195
- Duerbeck H. W., 1988, *A&A*, **197**, 148
- Evans A., Bode M. F., O’Brien T. J., Darnley M. J., 2008, *RS Ophiuchi (2006) and the Recurrent Nova Phenomenon*. *Astronomical Society of the Pacific Conference Series Vol. 401*
- Figueira J., José J., García-Berro E., Campbell S. W., García-Senz D., Mohamed S., 2018, *A&A*, **613**, A8
- Fitzpatrick E. L., 1986, *AJ*, **92**, 1068
- Fragner M. M., Nelson R. P., 2010, *A&A*, **511**, A77

- Gaposchkin C. H. P., 1957, The Galactic Novae
- Gehrels N., et al., 2004, *ApJ*, **611**, 1005
- Gill C. D., O'Brien T. J., 1999, *MNRAS*, **307**, 677
- Gill C. D., O'Brien T. J., 2000, *MNRAS*, **314**, 175
- Girardi L., 2016, *ARA&A*, **54**, 95
- Gutierrez J., Garcia-Berro E., Iben Icko J., Isern J., Labay J., Canal R., 1996, *ApJ*, **459**, 701
- Harman D. J., O'Brien T. J., 2003, *MNRAS*, **344**, 1219
- Henden A. A., Levine S. E., Terrell D., Smith T. C., Welch D., 2012, *Journal of the American Association of Variable Star Observers (JAAVSO)*, **40**, 430
- Henze M., Meusinger H., Pietsch W., 2008, *A&A*, **477**, 67
- Henze M., et al., 2014a, *A&A*, **563**, A2
- Henze M., Ness J. U., Darnley M. J., Bode M. F., Williams S. C., Shafter A. W., Kato M., Hachisu I., 2014b, *A&A*, **563**, L8
- Henze M., et al., 2015, *A&A*, **580**, A46
- Henze M., et al., 2018, *ApJ*, **857**, 68
- Hernanz M., José J., 2008, *New Astron. Rev.*, **52**, 386
- Hillebrandt W., Niemeyer J. C., 2000, *ARA&A*, **38**, 191
- Hillman Y., Prialnik D., Kovetz A., Shara M. M., 2016, *ApJ*, **819**, 168
- Hubble E. P., 1929, *ApJ*, **69**, 103
- Hutchings J. B., 1972, *MNRAS*, **158**, 177
- Kafka S., Williams R., 2011, *A&A*, **526**, A83
- Kalberla P. M. W., Burton W. B., Hartmann D., Arnal E. M., Bajaja E., Morras R., Pöppel W. G. L., 2005, *A&A*, **440**, 775
- Koornneef J., 1982, *A&A*, **107**, 247
- Krautter J., Oegelman H., Starrfield S., Wichmann R., Pfeffermann E., 1996, *ApJ*, **456**, 788
- Kuin P., 2014, UVOTPY: Swift UVOT grism data reduction (ascl:1410.004)
- Kuin N. P. M., et al., 2015, *MNRAS*, **449**, 2514
- Landolt A. U., 2009, *AJ*, **137**, 4186
- Liller W., 1990, *IAU Circ.*, **4961**, 2
- Liller W., Herald D., McNaught R. H., Pearce A., Seargent D. A. J., 1987, *IAU Circ.*, **4428**, 1
- Liller W., Shida R. Y., Jones A. F., 2004, *Information Bulletin on Variable Stars*, **5582**, 1
- Liszt H., 2014, *ApJ*, **780**, 10
- Livio M., Mazzali P., 2018, *Phys. Rep.*, **736**, 1
- Luyten W. J., 1927, *Harvard College Observatory Bulletin*, **847**, 8
- Markwardt C. B., 2009, in Bohlender D. A., Durand D., Dowler P., eds, *Astronomical Society of the Pacific Conference Series Vol. 411, Astronomical Data Analysis Software and Systems XVIII*. p. 251 ([arXiv:0902.2850](https://arxiv.org/abs/0902.2850))
- Mason K. O., Breeveld A., Hunsberger S. D., James C., Kennedy T. E., Roming P. W. A., Stock J., 2004a, in Flanagan K. A., Siegmund O. H. W., eds, *Society of Photo-Optical Instrumentation Engineers (SPIE) Conference Series Vol. 5165, Proc. SPIE*. pp 277–286, [doi:10.1117/12.503713](https://doi.org/10.1117/12.503713)
- Mason E., Ederoclite A., Stefanon M., dall T. H., Della Valle M., 2004b, *IAU Circ.*, **8424**, 2
- Mason E., Ederoclite A., Williams R. E., Della Valle M., Setiawan J., 2012, *A&A*, **544**, A149
- Mroz P., Udalski A., 2016, *The Astronomer's Telegram*, **8578**, 1
- Mroz P., Udalski A., 2018, *The Astronomer's Telegram*, **11384**, 1
- Mróz P., et al., 2014, *MNRAS*, **443**, 784
- Mróz P., et al., 2016, *ApJS*, **222**, 9
- Munari U., Moretti S., 2012, *Baltic Astronomy*, **21**, 22
- Munari U., Valisa P., 2014, *Contributions of the Astronomical Observatory Skalnaté Pleso*, **43**, 174
- Munari U., et al., 2012, *Baltic Astronomy*, **21**, 13
- Munari U., Henden A., Frigo A., Dallaporta S., 2014a, *Journal of Astronomical Data*, **20**, 4
- Munari U., et al., 2014b, *AJ*, **148**, 81
- Munari U., Walter F. M., Hamsch F. J., Frigo A., 2016, *Information Bulletin on Variable Stars*, **6162**, 1
- Mustel E. R., Boyarchuk A. A., 1970, *Ap&SS*, **6**, 183
- Ness J. U., et al., 2009, *AJ*, **137**, 4160
- Ness J. U., et al., 2013, *A&A*, **559**, A50
- Nichols J. S., Linsky J. L., 1996, *AJ*, **111**, 517
- Orio M., et al., 2013, *MNRAS*, **429**, 1342
- Osborne J. P., 2015, *Journal of High Energy Astrophysics*, **7**, 117
- Osborne J. P., et al., 2011, *ApJ*, **727**, 124
- Page K. L., Osborne J. P., Wagner R. M., Beardmore A. P., Shore S. N., Starrfield S., Woodward C. E., 2013, *ApJ*, **768**, L26
- Page K. L., et al., 2015a, *MNRAS*, **454**, 3108
- Page K. L., et al., 2015b, *MNRAS*, **454**, 3108
- Pagnotta A., Schaefer B. E., 2014, *ApJ*, **788**, 164
- Pagnotta A., Schaefer B. E., Xiao L., Collazzi A. C., Kroll P., 2009, *AJ*, **138**, 1230
- Pagnotta A., et al., 2015, *ApJ*, **811**, 32
- Pietrzyński G., et al., 2013, *Nature*, **495**, 76
- Pietrzyński G., et al., 2019, *Nature*, **567**, 200
- Pietsch W., 2010, *Astronomische Nachrichten*, **331**, 187
- Pietsch W., et al., 2007, *A&A*, **465**, 375
- Pojmanski G., 2002, *Acta Astron.*, **52**, 397
- Prialnik D., Kovetz A., 1995, *ApJ*, **445**, 789
- Ribeiro V. A. R. M., et al., 2009, *ApJ*, **703**, 1955
- Ribeiro V. A. R. M., Bode M. F., Darnley M. J., Barnsley R. M., Munari U., Harman D. J., 2013a, *MNRAS*, **433**, 1991
- Ribeiro V. A. R. M., Munari U., Valisa P., 2013b, *ApJ*, **768**, 49
- Roming P. W. A., et al., 2005, *Space Sci. Rev.*, **120**, 95
- Rosino L., 1964, *Annales d'Astrophysique*, **27**, 498
- Sala G., Hernanz M., 2005, *A&A*, **439**, 1061
- Schaefer B. E., 2010, *ApJS*, **187**, 275
- Schaefer B. E., Ringwald F. A., 1995, *ApJ*, **447**, L45
- Schwarz G. J., et al., 2011, *ApJS*, **197**, 31
- Schwarzenberg-Czerny A., 1996, *ApJ*, **460**, L107
- Sekiguchi K., Feast M. W., Whitelock P. A., Overbeek M. D., Wargau W., Jones J. S., 1988, *MNRAS*, **234**, 281
- Sekiguchi K., et al., 1989, *MNRAS*, **236**, 611
- Sekiguchi K., Stobie R. S., Buckley D. A. H., Caldwell J. A. R., 1990, *MNRAS*, **245**, 28P
- Shafter A. W., 2013, *AJ*, **145**, 117
- Shafter A. W., 2017, *ApJ*, **834**, 196
- Shafter A. W., et al., 2015, *ApJS*, **216**, 34
- Shara M. M., et al., 2016, *ApJS*, **227**, 1
- Shore S. N., 2012, *Bulletin of the Astronomical Society of India*, **40**, 185
- Shore S. N., Sonneborn G., Starrfield S. G., Hamuy M., Williams R. E., Cassatella A., Drechsel H., 1991, *ApJ*, **370**, 193
- Shore S. N., Starrfield S., Sonneborn G., 1996, *ApJ*, **463**, L21
- Shore S. N., Schwarz G. J., De Gennaro Aquino I., Augusteijn T., Walter F. M., Starrfield S., Sion E. M., 2013a, *A&A*, **549**, A140
- Shore S. N., De Gennaro Aquino I., Schwarz G. J., Augusteijn T., Cheung C. C., Walter F. M., Starrfield S., 2013b, *A&A*, **553**, A123
- Shore S. N., et al., 2016, *A&A*, **590**, A123
- Shore S. N., Kuin N. P., Mason E., De Gennaro Aquino I., 2018, *A&A*, **619**, A104
- Sievers J., 1970, *Information Bulletin on Variable Stars*, **448**, 1
- Smith J. A., et al., 2002, *AJ*, **123**, 2121
- Solf J., 1983, *ApJ*, **273**, 647
- Soraisam M. D., Gilfanov M., Wolf W. M., Bildsten L., 2016, *MNRAS*, **455**, 668
- Starrfield S., et al., 1988a, in *ESA Special Publication*. pp 167–170
- Starrfield S., Sparks W. M., Shaviv G., 1988b, *ApJ*, **325**, L35
- Starrfield S., Iliadis C., Timmes F. X., Hix W. R., Arnett W. D., Meakin C., Sparks W. M., 2012, *Bulletin of the Astronomical Society of India*, **40**, 419
- Starrfield S., Iliadis C., Hix W. R., 2016, *PASP*, **128**, 051001
- Tang S., et al., 2014, *ApJ*, **786**, 61
- Tisserand P., et al., 2007, *A&A*, **469**, 387

Udalski A., Szymanski M. K., Soszynski I., Poleski R., 2008, *Acta Astron.*, **58**, 69
Udalski A., Szymański M. K., Szymański G., 2015, *Acta Astron.*, **65**, 1
Verbunt F., 1982, *Space Sci. Rev.*, **32**, 379
Verbunt F., 1987, *A&AS*, **71**, 339
Walter F. M., Battisti A., Towers S. E., Bond H. E., Stringfellow G. S., 2012, *PASP*, **124**, 1057
Whelan J., Iben Icko J., 1973, *ApJ*, **186**, 1007
Williams R. E., Sparks W. M., Gallagher J. S., Ney E. P., Starrfield S. G., Truran J. W., 1981, *ApJ*, **251**, 221
Williams R. E., Hamuy M., Phillips M. M., Heathcote S. R., Wells L., Navarrete M., Duerbeck H. W., 2003, *Journal of Astronomical Data*, **9**, 3
Williams S. C., Darnley M. J., Bode M. F., Shafter A. W., 2016, *ApJ*, **817**, 143

Wolf W. M., Bildsten L., Brooks J., Paxton B., 2013, *ApJ*, **777**, 136
Woudt P. A., Ribeiro V. A. R. M., 2014, *Stella Novae: Past and Future Decades. Astronomical Society of the Pacific Conference Series Vol. 490*
Yaron O., Prialnik D., Shara M. M., Kovetz A., 2005, *ApJ*, **623**, 398

APPENDIX A: APPENDIX

This paper has been typeset from a $\text{T}_{\text{E}}\text{X}/\text{L}^{\text{A}}\text{T}_{\text{E}}\text{X}$ file prepared by the author.

Table A1. All known UV-optical spectra of N LMC 1968 ordered by day since respective outburst.

mission or instrument (1)	year eruption	midtime JD (d)	day since eruption	orbital phase (2)	ID and notes
CTIO/Argus	1990	2447936.6	0.0	0.19	discovery spectrum (3)
IUE	1990	2447938.51149	1.92	0.70	SWP38199
IUE	1990	2447938.55107	1.95	0.73	LWP17374
IUE	1990	2447938.56480	1.97	0.75	SWP38200
IUE	1990	2447939.01385	2.42	0.10	SWP38202
IUE	1990	2447939.03438	2.44	0.12	LWP17378
IUE	1990	2447939.23461	2.65	0.27	LWP17379
IUE	1990	2447939.26223	2.67	0.30	SWP38204
IUE	1990	2447939.28532	2.69	0.31	LWP17380
UVOT UVG	2016	2457410.78200	2.88	0.64	00045768005
UVOT UVG	2016	2457411.32973	3.43	0.07	00045768006
IUE	1990	2447940.44478	3.86	0.21-0.26	SWP38209
IUE	1990	2447940.47694	3.89	0.23-0.29	LWP17390
UVOT UVG	2016	2457411.77783	3.88	0.4260	00045768007
LCO IMACS	2016	2457411.5351	3.945	0.23	fits file
UVOT UVG	2016	2457411.91122	4.01	0.5315	00045768008
UVOT UVG	2016	2457412.97519	5.07	0.3730	00045768009
UVOT UVG	2016	2457413.12185	5.22	0.4890	00045768010
IUE	1990	2447942.34466	5.77	0.68-0.79	SWP38214
UVOT UVG	2016	2457414.04720	6.14	0.2209	00034302002
UVOT UVG	2016	2457415.11269	7.21	0.0636	00034302004
SAAO	1990	2447944.31	7.71	0.29	not recoverable
Mirranook Armidale	2016	2457415.9501	8.05	0.73	fits file
UVOT UVG	2016	2457416.03941	8.13	0.7966	00034302006
SAAO	1990	2447945.33	8.73	0.10	published
UVOT UVG	2016	2457416.70604	8.80	0.3239	00034302008
IUE	1990	2447945.50490	8.93	0.71-0.82	SWP38229
CTIO	1990	2447945.6029	9.00	0.31	fits file
FTS/FLOYDS	2016	2457417.1	9.2	0.63	fits file
IUE	1990	2447946.25125	9.69	0.74-0.91	SWP38231
UVOT VG	2016	2457417.63602	9.73	0.5940	00034302010
UVOT VG	2016	2457418.03603	10.13	0.3758	00034302012
SAAO	1990	2447948.29	11.69	0.44	not recoverable
SAAO	1990	2447952.36	15.76	0.66	published
IUE	1990	2447952.88444	16.35	0.95-0.20	SWP38284
LCO duPont	2016	2457427.6486	19.73	0.98	fits file
LCO duPont	2016	2457428.6344	20.72	0.76	fits file
LCO duPont	2016	2457429.5827	21.67	0.51	fits file
IUE	1990	2447970.87319	34.35	0.15-0.45	SWP38394
IUE	1990	2447976.81065	40.35	0.72-0.27	SWP38439
IUE	1990	2447977.81134	41.35	0.73-0.28	LWP17625
LCO IMACS	2016	2457476.5447	68.64	0.65	fits file
LCO IMACS	2016	2457476.5690	68.67	0.67	fits file

¹ Spectral ranges per instrument:

IUE SWP is 1150–2000Å; IUE LWP is 1800–3300Å, UVOT UVGRISM is 1700–5000Å; UVOT VGRISM is 2900–6600Å; CTIO is 3500–7700Å; Magellan/IMACS is 4000–9000Å; SAAO is 3500–7200Å; FTS/Floyds 3300–11000Å.

² for the 1990 eruption the orbital phase uncertainty is 0.15 and based on Eq. 2The range in phase is due to long observations, e.g. for IUE, otherwise ≤ 0.02 .³ This has been lost, unfortunately. Personal communication with Mike Shara and Bob Williams.

Table A2. Swift UVOT Grism exposures.

Mid-time ¹ JD(+2450000)	Day ²	Orbital ¹ phase	Swift OBSID	Roll deg	Anchor ⁵ (X,Y)pix	Exposure time (s)	UV/V grism	uvw1 ³	Scale ⁴ factor
7410.78200	2.88	.6383	00045768005	219.1	1046, 875	285.3	UV	13.642	1.00
7411.32973	3.43	.0716	00045768006	223.0	1235, 925	405.0	UV	13.723	1.08
7411.77783	3.88	.4260	00045768007	216.0	1198,1034	282.3	UV	13.697	1.05
7411.91122	4.01	.5315	00045768008	220.0	1263, 945	285.9	UV	13.694	1.05
7412.97519	5.07	.3730	00045768009	217.0	1270, 834	294.3	UV	14.363	1.95
7413.12185	5.22	.4890	00045768010	221.1	1106, 886	398.8	UV	14.624	2.48
7414.04720	6.14	.2209	00034302002	237.0	1130,1613	892.5	UV	15.614	6.16
7415.11269	7.21	.0636	00034302004	222.0	972,1620	946.6	UV	15.822	7.46
7416.03941	8.13	.7966	00034302006	223.0	1034,1590	999.7	UV	15.884	7.90
7416.70604	8.80	.3239	00034302008	223.0	952,1636	892.5	UV	16.156	10.15
7417.63602	9.73	.5940	00034302010	232.0	1114,1662	892.5	V	16.586	15.08
7418.03603	10.13	.3758	00034302012	232.0	1101,1638	892.5	V	16.675	16.37

¹ mid-time of exposure² days since estimated time of eruption JD 2457407.9³ uvw1 magnitude interpolated from a spline fit to the light curve⁴ flux scale factor derived from uvw1 light curve⁵ the anchor is defined by the position in the first order spectrum at 260 nm (UV) or 420 nm (V)

Table A3. Photometry from 10 days before to 50 days after the 2016 eruption of N LMC 1968^a

Date ^a (MJD)	mag	mag error	Orbital ^c phase	instrument and filter	phot. system	Date ^a (MJD)	mag	mag error	Orbital ^c phase	instrument and filter	phot. system
7399.24670	19.297	0.042	0.91014	OGLE I	Vega	7416.18044	16.216	0.004	0.30360	OGLE I	Vega
7404.23630	19.422	0.042	0.85658	OGLE I	Vega	7416.21044	16.167	0.064	0.32733	UVOT UVW2	AB
7408.20942	99.999	9.999	0.99906	OGLE I	Vega	7417.03829	16.251	0.043	0.98211	ANS	Vega
7410.04082	12.820	0.005	0.44758	Andicam I	Vega	7417.03829	16.780	0.019	0.98211	ANS	Vega
7410.04157	13.298	0.004	0.44817	Andicam B	Vega	7417.03829	17.075	0.028	0.98211	ANS	Vega
7410.05324	13.556	0.008	0.45740	Andicam V	Vega	7417.13390	16.951	0.016	0.05773	Andicam I	Vega
7410.05391	12.605	0.005	0.45793	Andicam R	Vega	7417.13569	17.117	0.009	0.05915	Andicam B	Vega
7410.17573	12.774	0.056	0.55428	ANS	Vega	7417.13744	17.225	0.017	0.06053	Andicam V	Vega
7410.17573	13.211	0.032	0.55428	ANS	Vega	7417.13869	16.809	0.015	0.06152	Andicam R	Vega
7410.17573	13.228	0.028	0.55428	ANS	Vega	7417.14031	16.660	0.053	0.06279	UVOT UVW1	AB
7410.21081	12.930	0.003	0.58202	OGLE I	Vega	7417.52781	16.548	0.042	0.36928	UVOT UVW1	AB
7410.27711	13.643	0.023	0.63446	UVOT UVW1	AB	7417.54031	16.738	0.055	0.37917	UVOT UVW1	AB
7410.82572	13.710	0.027	0.06838	UVOT UVW1	AB	7418.08238	15.981	0.034	0.80791	ANS	Vega
7411.17503	13.110	0.029	0.34466	ANS	Vega	7418.08238	16.408	0.015	0.80791	ANS	Vega
7411.17503	13.573	0.013	0.34466	ANS	Vega	7418.08238	16.571	0.008	0.80791	ANS	Vega
7411.17503	13.628	0.022	0.34466	ANS	Vega	7418.12675	16.676	0.014	0.84301	Andicam I	Vega
7411.27294	13.647	0.023	0.42210	UVOT UVW1	AB	7418.12850	16.904	0.007	0.84439	Andicam B	Vega
7411.40628	13.793	0.024	0.52756	UVOT UVW1	AB	7418.13025	16.965	0.013	0.84578	Andicam V	Vega
7412.06793	13.868	0.012	0.05088	Andicam I	Vega	7418.13150	16.719	0.013	0.84677	Andicam R	Vega
7412.06864	14.110	0.007	0.05145	Andicam B	Vega	7418.45558	16.740	0.097	0.10309	UVOT UVW1	AB
7412.06939	14.316	0.016	0.05204	Andicam V	Vega	7419.10888	16.940	0.015	0.61981	Andicam I	Vega
7412.07005	13.825	0.011	0.05256	Andicam R	Vega	7419.11063	17.161	0.008	0.62119	Andicam B	Vega
7412.08291	13.768	0.003	0.06273	OGLE I	Vega	7419.11238	17.141	0.015	0.62258	Andicam V	Vega
7412.17229	13.808	0.040	0.13342	ANS	Vega	7419.11363	16.940	0.015	0.62357	Andicam R	Vega
7412.17229	14.030	0.023	0.13342	ANS	Vega	7419.15646	-1.000	-1.000	0.65744	ANS	Vega
7412.17229	14.117	0.019	0.13342	ANS	Vega	7419.15646	16.570	0.018	0.65744	ANS	Vega
7412.24426	13.774	0.012	0.19035	Andicam I	Vega	7419.15646	16.806	0.016	0.65744	ANS	Vega
7412.25706	14.180	0.015	0.20047	Andicam V	Vega	7420.04870	-1.000	-1.000	0.36314	ANS	Vega
7412.25797	13.620	0.012	0.20119	Andicam R	Vega	7420.04870	16.610	0.016	0.36314	ANS	Vega
7412.47017	14.052	0.024	0.36902	UVOT UVW1	AB	7420.04870	16.770	0.038	0.36314	ANS	Vega
7412.61739	14.902	0.031	0.48547	UVOT UVW1	AB	7420.11907	16.882	0.017	0.41879	Andicam I	Vega
7413.16938	14.257	0.058	0.92206	ANS	Vega	7420.12086	17.151	0.008	0.42021	Andicam B	Vega
7413.16938	14.531	0.034	0.92206	ANS	Vega	7420.12261	17.152	0.015	0.42159	Andicam V	Vega
7413.16938	14.597	0.030	0.92206	ANS	Vega	7420.12386	16.869	0.016	0.42258	Andicam R	Vega
7413.17357	14.234	0.003	0.92537	OGLE I	Vega	7420.25142	16.710	0.026	0.52348	UVOT UVW1	AB
7413.53753	14.515	0.024	0.21323	UVOT UVW2	AB	7420.65281	16.884	0.031	0.84095	UVOT UVW1	AB
7413.55142	14.574	0.030	0.22422	UVOT UVW2	AB	7421.03317	16.153	0.045	0.14179	ANS	Vega
7414.13745	14.791	0.048	0.68774	Andicam I	Vega	7421.03317	16.739	0.024	0.14179	ANS	Vega
7414.14558	15.311	0.013	0.69417	Andicam B	Vega	7421.03317	16.900	0.032	0.14179	ANS	Vega
7414.14966	14.998	0.009	0.69739	Andicam V	Vega	7421.15504	16.899	0.016	0.23818	Andicam I	Vega
7414.15374	14.715	0.014	0.70062	Andicam R	Vega	7421.15679	17.028	0.007	0.23956	Andicam B	Vega
7414.16670	14.390	0.072	0.71087	ANS	Vega	7421.15854	17.035	0.014	0.24095	Andicam V	Vega
7414.16670	14.586	0.028	0.71087	ANS	Vega	7421.15979	16.885	0.015	0.24194	Andicam R	Vega
7414.16670	14.839	0.071	0.71087	ANS	Vega	7421.51739	16.646	0.031	0.52478	UVOT UVW1	AB
7414.26437	14.501	0.003	0.78812	OGLE I	Vega	7421.58406	16.601	0.030	0.57751	UVOT UVW1	AB
7414.60489	15.596	0.039	0.05745	UVOT UVM2	AB	7422.04978	16.396	0.043	0.94586	ANS	Vega
7414.61739	15.732	0.036	0.06733	UVOT UVW2	AB	7422.04978	16.812	0.039	0.94586	ANS	Vega
7415.15130	15.604	0.008	0.48962	Andicam I	Vega	7422.04978	17.066	0.061	0.94586	ANS	Vega
7415.15305	15.983	0.006	0.49101	Andicam B	Vega	7422.09426	17.516	0.022	0.98104	Andicam I	Vega
7415.15484	16.013	0.010	0.49242	Andicam V	Vega	7422.09605	17.846	0.012	0.98246	Andicam B	Vega
7415.15605	15.573	0.008	0.49338	Andicam R	Vega	7422.09780	17.769	0.022	0.98384	Andicam V	Vega
7415.16300	15.396	0.003	0.49888	OGLE I	Vega	7422.09905	17.513	0.022	0.98483	Andicam R	Vega
7415.52989	15.873	0.031	0.78906	UVOT UVW1	AB	7423.18165	17.034	0.018	0.84110	Andicam I	Vega
7415.54447	16.009	0.039	0.80059	UVOT UVW2	AB	7423.18340	17.343	0.010	0.84248	Andicam B	Vega
7416.15497	16.253	0.014	0.28346	Andicam I	Vega	7423.18515	17.324	0.019	0.84386	Andicam V	Vega
7416.15677	16.565	0.008	0.28488	Andicam B	Vega	7423.18640	17.249	0.019	0.84485	Andicam R	Vega
7416.15852	16.591	0.014	0.28627	Andicam V	Vega	7424.04142	-1.000	-1.000	0.52112	ANS	Vega
7416.15977	16.193	0.013	0.28726	Andicam R	Vega	7424.04142	16.656	0.020	0.52112	ANS	Vega
7416.16446	15.929	0.132	0.29096	ANS	Vega	7424.04142	16.956	0.022	0.52112	ANS	Vega
7416.16446	16.228	0.054	0.29096	ANS	Vega	7424.11649	16.952	0.016	0.58049	Andicam I	Vega
7416.16446	16.260	0.071	0.29096	ANS	Vega						

Table A3 – continued

Table A3 – continued

Date ^a (MJD)	mag	mag error	Orbital ^c phase	instrument and filter	phot. system	Date ^a (MJD)	mag	mag error	Orbital ^c phase	instrument and filter	phot. system
7424.11824	17.066	0.008	0.58188	Andicam B	Vega	7439.61190	18.517	0.053	0.83633	UVOT UVW1	AB
7424.11999	17.043	0.015	0.58326	Andicam V	Vega	7440.08900	18.407	0.046	0.21368	Andicam I	Vega
7424.12124	16.963	0.016	0.58425	Andicam R	Vega	7440.09075	18.555	0.058	0.21507	Andicam B	Vega
7424.12285	16.833	0.006	0.58552	OGLE I	Vega	7440.09250	18.558	0.063	0.21645	Andicam V	Vega
7425.12780	16.926	0.017	0.38037	Andicam I	Vega	7440.09375	18.287	0.059	0.21744	Andicam R	Vega
7425.12955	17.170	0.008	0.38175	Andicam B	Vega	7440.27579	18.234	0.055	0.36142	UVOT UVW1	AB
7425.13134	17.149	0.016	0.38317	Andicam V	Vega	7440.66955	18.477	0.114	0.67285	UVOT UVW1	AB
7425.13255	17.025	0.018	0.38412	Andicam R	Vega	7441.02710	18.946	0.048	0.95565	Andicam I	Vega
7425.16908	16.887	0.006	0.41302	OGLE I	Vega	7441.02885	19.208	0.078	0.95704	Andicam B	Vega
7426.15560	17.134	0.021	0.19329	Andicam I	Vega	7441.03064	19.505	0.090	0.95845	Andicam V	Vega
7426.15735	17.224	0.009	0.19467	Andicam B	Vega	7441.03193	19.299	0.068	0.95948	Andicam R	Vega
7426.15914	17.192	0.017	0.19609	Andicam V	Vega	7441.10293	18.912	0.035	0.01563	OGLE I	Vega
7426.16035	17.093	0.019	0.19705	Andicam R	Vega	7441.26816	18.558	0.054	0.14632	UVOT UVW1	AB
7426.16622	16.974	0.008	0.20169	OGLE I	Vega	7441.73413	18.353	0.051	0.51487	UVOT UVW1	AB
7427.14781	17.542	0.009	0.97806	OGLE I	Vega	7442.04882	18.085	0.036	0.76377	Andicam I	Vega
7428.10171	17.178	0.018	0.73254	Andicam I	Vega	7442.05057	18.749	0.051	0.76516	Andicam B	Vega
7428.10346	17.414	0.009	0.73392	Andicam B	Vega	7442.05236	18.418	0.058	0.76657	Andicam V	Vega
7428.10521	17.378	0.017	0.73531	Andicam V	Vega	7442.05357	18.637	0.050	0.76753	Andicam R	Vega
7428.10646	17.250	0.019	0.73629	Andicam R	Vega	7442.39803	18.703	0.060	0.03997	UVOT UVW1	AB
7428.15238	17.202	0.007	0.77261	OGLE I	Vega	7442.59942	18.553	0.061	0.19925	UVOT UVW1	AB
7429.11102	17.266	0.020	0.53083	Andicam I	Vega	7443.06192	18.506	0.051	0.56506	UVOT UVW1	AB
7429.11277	17.449	0.010	0.53221	Andicam B	Vega	7443.09063	18.443	0.025	0.58777	Andicam I	Vega
7429.11452	17.458	0.018	0.53360	Andicam V	Vega	7443.09354	18.653	0.030	0.59007	Andicam B	Vega
7429.11577	17.358	0.020	0.53459	Andicam R	Vega	7443.09646	18.646	0.026	0.59238	Andicam V	Vega
7429.16175	17.156	0.006	0.57096	OGLE I	Vega	7443.09942	18.420	0.024	0.59472	Andicam R	Vega
7431.11144	17.391	0.007	0.11303	OGLE I	Vega	7443.11736	18.283	0.015	0.60891	OGLE I	Vega
7431.44867	17.194	0.036	0.37976	UVOT UVW1	AB	7443.12006	18.260	0.015	0.61105	OGLE I	Vega
7431.51464	17.184	0.034	0.43194	UVOT UVW1	AB	7443.65915	18.707	0.052	0.03743	UVOT UVW1	AB
7431.84659	17.529	0.040	0.69448	UVOT UVW1	AB	7444.05776	18.544	0.048	0.35271	UVOT UVW1	AB
7431.91256	17.453	0.037	0.74666	UVOT UVW1	AB	7444.65498	18.769	0.058	0.82507	UVOT UVW1	AB
7432.12850	17.775	0.010	0.91746	OGLE I	Vega	7445.10716	18.410	0.021	0.18271	OGLE I	Vega
7432.37992	17.470	0.036	0.11632	UVOT UVW1	AB	7445.58555	18.727	0.058	0.56108	UVOT UVW1	AB
7432.77229	17.344	0.028	0.42665	UVOT UVW1	AB	7446.02288	18.822	0.022	0.90698	Andicam I	Vega
7433.30354	17.717	0.034	0.84683	UVOT UVW1	AB	7446.02580	19.104	0.013	0.90929	Andicam B	Vega
7433.83410	17.547	0.058	0.26647	UVOT UVW1	AB	7446.02876	19.037	0.013	0.91163	Andicam V	Vega
7434.10890	17.560	0.009	0.48382	OGLE I	Vega	7446.03167	18.932	0.014	0.91394	Andicam R	Vega
7434.37299	17.592	0.034	0.69270	UVOT UVW1	AB	7446.58208	18.709	0.053	0.34928	UVOT UVW1	AB
7434.43132	17.762	0.055	0.73883	UVOT UVW1	AB	7447.04343	18.760	0.021	0.71418	Andicam I	Vega
7435.14184	17.698	0.010	0.30081	OGLE I	Vega	7447.04635	19.181	0.013	0.71649	Andicam B	Vega
7435.22646	17.722	0.034	0.36774	UVOT UVW1	AB	7447.04931	18.919	0.012	0.71883	Andicam V	Vega
7435.69174	17.962	0.034	0.73574	UVOT UVW1	AB	7447.05226	18.733	0.013	0.72116	Andicam R	Vega
7436.29105	18.058	0.034	0.20976	UVOT UVW1	AB	7447.13940	18.686	0.018	0.79008	OGLE I	Vega
7436.82578	17.938	0.035	0.63269	UVOT UVW1	AB	7448.02695	18.666	0.020	0.49207	Andicam I	Vega
7437.11450	18.227	0.015	0.86105	OGLE I	Vega	7448.02987	19.180	0.012	0.49438	Andicam B	Vega
7437.13404	18.188	0.030	0.87650	Andicam I	Vega	7448.03278	18.816	0.012	0.49668	Andicam V	Vega
7437.13579	18.591	0.042	0.87789	Andicam B	Vega	7448.03574	18.747	0.013	0.49902	Andicam R	Vega
7437.13759	18.557	0.051	0.87931	Andicam V	Vega	7448.57723	18.717	0.063	0.92731	UVOT UVW1	AB
7437.13879	18.450	0.043	0.88026	Andicam R	Vega	7449.01826	18.687	0.026	0.27613	Andicam I	Vega
7437.74939	17.938	0.040	0.36321	UVOT UVW1	AB	7449.02118	19.233	0.014	0.27844	Andicam B	Vega
7438.08501	18.074	0.033	0.62866	Andicam I	Vega	7449.02413	18.792	0.014	0.28077	Andicam V	Vega
7438.08680	18.284	0.036	0.63008	Andicam B	Vega	7449.02705	18.831	0.016	0.28308	Andicam R	Vega
7438.08855	18.322	0.047	0.63146	Andicam V	Vega	7449.10640	18.584	0.049	0.34585	UVOT UVW1	AB
7438.08980	18.169	0.040	0.63245	Andicam R	Vega	7449.12580	18.459	0.022	0.36119	OGLE I	Vega
7438.28134	18.310	0.054	0.78394	UVOT UVW1	AB	7449.57168	18.710	0.054	0.71385	UVOT UVW1	AB
7438.75426	18.231	0.048	0.15799	UVOT UVW1	AB	7450.01960	18.771	0.023	0.06813	Andicam I	Vega
7439.03049	18.436	0.034	0.37647	Andicam I	Vega	7450.02252	19.008	0.012	0.07044	Andicam B	Vega
7439.03224	18.409	0.026	0.37785	Andicam B	Vega	7450.02547	18.906	0.013	0.07277	Andicam V	Vega
7439.03399	18.750	0.054	0.37924	Andicam V	Vega	7450.02839	18.871	0.015	0.07508	Andicam R	Vega
7439.03524	18.134	0.049	0.38023	Andicam R	Vega	7450.03835	18.803	0.062	0.08296	UVOT UVW1	AB
7439.07718	18.113	0.046	0.41340	UVOT UVW1	AB	7450.56752	18.696	0.053	0.50150	UVOT UVW1	AB
7439.14844	18.109	0.016	0.46976	OGLE I	Vega	7451.10166	18.873	0.023	0.92396	Andicam I	Vega

□

Table A3 – *continued*

Date ^a (MJD)	mag	mag error	Orbital ^c phase	instrument and filter	phot. system
7451.10462	19.208	0.014	0.92630	Andicam B	Vega
7451.10758	19.187	0.013	0.92865	Andicam V	Vega
7451.11049	19.006	0.014	0.93095	Andicam R	Vega
7451.16683	19.312	0.076	0.97551	UVOT UVW1	AB
7452.02922	18.656	0.024	0.65760	Andicam I	Vega
7452.03213	18.898	0.012	0.65990	Andicam B	Vega
7452.03509	18.904	0.012	0.66224	Andicam V	Vega
7452.03801	18.889	0.015	0.66455	Andicam R	Vega
7453.04974	18.816	0.021	0.46476	Andicam I	Vega
7453.05269	19.243	0.013	0.46709	Andicam B	Vega
7453.05561	18.963	0.013	0.46940	Andicam V	Vega
7453.05853	18.963	0.015	0.47171	Andicam R	Vega
7453.10025	18.718	0.019	0.50471	OGLE I	Vega
7453.49185	19.068	0.110	0.81444	UVOT UVM2	AB
7453.49532	18.899	0.109	0.81719	UVOT UVW1	AB
7453.49671	18.253	0.104	0.81829	UVOT U	AB
7453.49810	19.300	0.086	0.81939	UVOT UVW2	AB
7454.03666	19.264	0.088	0.24535	Andicam B	Vega
7454.03958	19.125	0.079	0.24766	Andicam V	Vega
7454.04249	18.981	0.029	0.24997	Andicam R	Vega
7455.88284	18.955	0.156	0.70556	UVOT UVM2	AB
7455.88423	18.822	0.160	0.70666	UVOT UVW1	AB
7455.88492	18.074	0.153	0.70721	UVOT U	AB
7455.88562	19.110	0.112	0.70775	UVOT UVW2	AB
7455.94881	18.834	0.098	0.75774	UVOT UVM2	AB
7455.95159	18.715	0.100	0.75993	UVOT UVW1	AB
7455.95367	18.417	0.122	0.76158	UVOT U	AB
7455.95506	19.098	0.076	0.76268	UVOT UVW2	AB
7456.01465	18.848	0.025	0.80981	Andicam I	Vega
7456.01757	19.081	0.014	0.81212	Andicam B	Vega
7456.02053	19.213	0.015	0.81446	Andicam V	Vega
7456.02348	18.934	0.016	0.81679	Andicam R	Vega
7457.01450	18.757	0.023	0.60062	Andicam I	Vega
7457.01746	19.018	0.013	0.60296	Andicam B	Vega
7457.02042	18.965	0.013	0.60530	Andicam V	Vega
7457.02338	18.739	0.013	0.60765	Andicam R	Vega
7457.11303	18.722	0.022	0.67856	OGLE I	Vega
7457.41619	18.944	0.089	0.91833	UVOT UVM2	AB
7457.42035	18.860	0.089	0.92163	UVOT UVW1	AB
7457.42313	18.644	0.103	0.92382	UVOT U	AB
7457.42452	19.066	0.063	0.92492	UVOT UVW2	AB

^a The full set of collected photometric and spectroscopic data on N LMC 1968 will be submitted to the IAU astronomical data centers.^b time of exposure; mid-time if possible.^c from eq. 2.